Porous g-C3N4-based nanoarchitectures by playing with sustainable precursors: Role of urea/melamine ratio on the structure/properties relationship

Published version:

DOI:10.1016/j.jallcom.2024.175053

[Paolo Negro, Federico Cesano, Alessandro Damin, Rosaria Brescia, Domenica Scarano, Porous g-C_3N_4-based nanoarchitectures by playing with sustainable precursors: Role of urea/melamine ratio on the structure/properties relationship, Journal of Alloys and Compounds Volume 1002, 15 October 2024, 175053a, DOI: 10.1016/j.jallcom.2024.175053]

Porous g-C_3N_4-based nanoarchitectures by playing with sustainable precursors: role of urea/melamine ratio on the structure/properties relationship.

Paolo Negro*[1], Federico Cesano[1], Alessandro Damin[1], Rosaria Brescia[2] and Domenica Scarano*[1]

[1]*Chemistry Department of Excellence and NIS (Nanomaterial for Industry and Sustainability) Interdepartmental Centre, University of Torino & INSTM-UdR Torino, Via P. Giuria 7, 10125 Torino, Italy*

[2]*Electron Microscopy Facility, Istituto Italiano di Tecnologia, Via Morego 30, 16163 Genova, Italy*

Keywords: g-C_3N_4; dual precursors; structure/morphological properties; porosity; optical properties; vibrational properties

Abstract

In this study, porous g-C_3N_4 based nanoarchitectures were obtained by a facile and effective in-situ synthesis method, that entailed the thermal treatment of different melamine (M) and urea (U) precursor mass ratios (in particular M/U = 50:50, 20:80), which were then compared with g-C_3N_4 obtained from pure M and U. The role of the melamine/urea mass ratio on morphology, structure, BET surface area, porosity, optical and vibrational properties of the g-C_3N_4 -based materials, was analysed in detail by means of many characterization techniques, including FESEM, AFM imaging, XRD, HRTEM, Raman, FTIR, UV and PL spectroscopies, BET and TGA analyses. It will be shown that samples obtained from different M and U precursor mass ratios combine the advantage of high thermal stability and significant reaction yields, which are due to melamine action, and greatly improved surface area and short migration paths, which are due to urea effect, thus providing the suitable conditions for charge transfer within the interfaces. The results may shed light on effective improvements in the structure/properties of g-C_3N_4 based nanoarchitectures, aiming at peculiar functional materials.

**Corresponding authors:*

E-mail address: pa.negro@unito.it *(Paolo Negro)*

E-mail address: domenica.scarano@unito.it *(Domenica Scarano)*

1. Introduction

Layered materials, also known as 2D materials, constitute a class of materials consisting of individual atomic or molecular layers, resulting in a two-dimensional structure [1]. Common examples of layered materials include graphene, which comprises a single layer of carbon atoms arranged in a honeycomb lattice, transition metal dichalcogenides (TMDs), consisting of layers of transition metal atoms sandwiched between chalcogen atoms (e.g., MoS_2, WSe_2) [2], and other graphene analogous, including Silicene, Phosphorene, boron nitride (BN), and graphitic carbon nitride (g-C_3N_4) [3]. In recent years the research in the field of 2D materials forming homojunctions (i.e., two adjacent structure domains of the same semiconductor material) [4,5] or heterojunctions (i.e., combination of two or more materials, e.g. MoS_2/graphene oxide, MoS_2/TiO_2, etc.) [6,7] has been very active. The ability of these junctions to confine electrons and holes to specific regions within the semiconductor structure (leading to, *e.g.*, enhanced carrier mobility, reduced electron-hole recombination, and improved device efficiency) and to modify the energy band gap makes them particularly attractive [8,9].

As for g-C_3N_4, it is a layered material that consists of stacked layers of carbon and nitrogen atoms arranged in a hexagonal lattice structure. These layers are composed of tri-s-triazine units, forming planar honeycomb layers that are weakly bound together by van der Waals forces. g-C_3N_4, a polymeric metal-free semiconductor, has been considered a challenging material, due to its thermal and chemical stability, non-toxicity, tuneable band gap and visible light activity, but also due to its environmentally friendly and sustainable properties [10,11]. Hence, widespread applications, including removal of toxic metal ions, degradation of dye pollutants, selective organic transformation to fine chemicals, photocatalytic hydrogen and ammonia production, carbon dioxide reduction, metal-free organic syntheses, water splitting, solar light-driven photo-redox catalysis, photoelectric conversion as well fuel cells have been developed [12-19]. Based on combined computation and experimental studies [20-22], the g-C_3N_4 complex layered structure, made by highly condensed g-C_3N_4 domains embedded in a framework of partially condensed strings, that is, the melon structure, has been well highlighted, also considering the role of the interactions between layers and rows in affecting the polymerization degree. Due to the heptazine-based architecture, g-C_3N_4 has a π-conjugated electronic structure, responsible for the visible light absorption at about 460 nm, which explains the typical pale-yellow colour [22].

Besides the aforementioned chemical inertness, that is responsible for the lack of reactivity to many conventional solvents [16,23], other drawbacks concerning the photocatalytic activity, should be then considered, including the high recombination rate of the photoinduced electron–hole pairs, the poor charge carrier mobility, the low specific surface area.

To overcome such drawbacks, heterojunctions or composite structures with innovative architectures made by *g*-C_3N_4 combined with metals or other semiconductors have been developed, aiming at improving the surface properties, the surface area, *etc.,* then the charge separation at the interfaces and the lifetime of the photoinduced charge carriers [21,22,24-34] .

Taking into account the fact that the energy gaps of g-C_3N_4 derived from different nitrogen rich precursors are quite similar [35], forming g-C_3N_4/g-C_3N_4 metal-free homojunctions can provide alternative ways to address the limits of *g*-C_3N_4 itself. As a matter of fact, there is an extensive literature on the coupling of two *g*-C_3N_4 coming from environment-friendly N-containing precursors, via not expensive and easy synthesis methods [36]. Concerning this, it is well known that the peculiar properties of g-C_3N_4/g-C_3N_4 interfaces are strongly depending on the synthesis processes, *i.e.* on the different precursors and on their ratio, on the reaction rates and/or temperatures, which are all affecting the condensation degree, the stacking order, the formation of defects, as well as the band gap junctions [22,24]. Although several thermal condensation processes, starting from single nitrogen-rich carbon-based precursors such as dicyanamide [18,37-39], cyanamide [40-42], melamine [43-46], urea [47-49], thiourea [50-53] and ammonium thiocyanate [54] have been carried out, the role of the two N-containing precursors at once and the effect of their ratios on the photocatalytic property of the g-C_3N_4/g-C_3N_4 metal-free homojunction, at molecular level, are still unclear [36,55]. In this respect, some photocatalytic mechanisms, including the type II, Z-scheme and S-Scheme ones, have been proposed to explain the charge transfer routes between the conduction band (CB) and the valence band (VB) of g-C_3N_4-based 2D/2D homojunctions [56,57].

However, the enhanced effects of isotype homojunctions obtained from thiourea/urea or urea/dicyanamide or cyanamide/urea have been already ascribed, by the way, to higher surface area and then to more available active sites for the absorption of reactants, to thinner layer thickness and to porous nanostructures, which allow the photogenerated charges to cover shorter distances, then to reach faster the surface. More in detail, the effective interfacial contact in 2D/2D structure combines both the advantages. *i.e.* high surface area and short migration routes, thus providing the suitable conditions for charge transfer within the interfaces [36,55,56,58,59].

In this contribution, g-C_3N_4-based structures, obtained by a facile and effective *in situ* synthesis method, that entailed the thermal treatment of different melamine/urea precursor ratios, were compared with g-C_3N_4 as obtained from melamine and urea pristine precursors. To this end, in-depth analysis on the role of the melamine/urea mass ratios on morphology, structure, BET surface area, porosity, optical and vibrational properties of the obtained materials, was provided. On this matter, also the mixed nature of the g-C_3N_4 system alone, made of condensed g-C_3N_4 domains embedded in a less condensed “melon-like” framework, should be taken into account [20].

The aim was to determine the most effective urea/melamine mass ratios for synthesizing g-C_3N_4 based systems, from sustainable precursors through simple and environmentally friendly synthesis methods, to be exploited for large scale applications.

Concerning this, the photocatalytic efficiency of all samples towards methylene blue (MB) photodegradation, as a model system for organic contaminants, has been investigated. Due to its complex structure, the MB cationic dye is non-degradable, thus causing long-term water pollution [60]. Along these themes, in this contribution the role of urea/melamine precursors ratio on the peculiar photocatalytic performances was also highlighted.

2. Materials and Methods

2.1. Materials and synthesis methods

Melamine ($C_3H_6N_6$, Sigma-Aldrich Melamine 99% M2659) and urea powders (CH_4N_2O, Merck art. 8487, analytical grade) were used as precursors, as received without further purification processes. In this study, different g-C_3N_4 samples were obtained via thermal polymerization of a mixture of urea and melamine, about 1.5 grams in total mass, with different mass ratios (*i.e.,* 98:2 (U_{98}-C_3N_4), 90:10 (U_{90}-C_3N_4), 80:20 (U_{80}-C_3N_4) and 50:50 (U_{50}-C_3N_4) of urea and melamine respectively), and compared with two g-C_3N_4 samples, as obtained from single precursors, *i.e.* from pure melamine (M-C_3N_4) and pure urea (U-C_3N_4), respectively. Concerning U_{98}-C_3N_4 and U_{90}-C_3N_4, same results are shown in supporting information, for sake of brevity. More in detail, the suitable amount of powder precursors was grinded and mixed for a while in a mortar, to ensure the uniform distribution of the before mentioned mass ratios. Then, the powders were introduced in ceramic crucibles and wrapped with aluminium foil to avoid the leakage of the precursors during heating. The crucibles have been heated up 1°C per minute in a muffle furnace (Nabertherm B400) to a temperature of 550°C and kept for 2h. After natural cooling at room temperature, the samples were grinded in a mortar and the collected pale-yellow powders were weighed to carry out a preliminary evaluation of the reaction yields, (Table 1 and Figure S1).

2.2. Characterization methods

Morphology, structure and spectroscopic properties of the obtained samples were investigated, by means of the following techniques.

Field Emission Scanning Electron Microscopy (FESEM) analyses were carried out by using FIB-FESEM/EBSD/TOF-SIMS Tescan S9000G microscope. In order to avoid any charging effect, the samples were coated with a chromium layer (Bal-tec SCD050 sputter coater) 5 nm in thickness, before performing the analysis.

Atomic Force Microscopy (AFM) analyses were performed in the Intermittent-Contact (IC) mode by means of a modified Nanosurf Easyscan2 AFM instrument, equipped with a 10 μm scan-head, inside a shielded and acoustically insulated enclosure on a high-performance anti-vibration platform.

Bright Field Transmission Electron Microscopy (BF-TEM) overview images and *Selected Area Electron Diffraction (SAED)* patterns were collected via a Tecnai F20 (FEI), a 200 kV TEM with a Schottky emitter.

High Resolution Transmission Electron Microscopy (HRTEM) was carried out using an image-Cs-corrected JEOL JEM-2200FS TEM (Schottky emitter), operated at 200 kV and equipped with an in-column imaging filter (Ω-type). The microscope is equipped with a direct electron detection (DED) camera (Gatan K2 Summit), which was used for HRTEM analyses to have a larger field-of-view at a lower dose rate in HRTEM mode.

Concerning *TEM specimen preparation*, a spatula tip of powder for each sample was added to isopropanol, sonicated (10 min.) and drop-cast onto holey carbon on Cu grids.

X-ray diffraction (XRD) patterns were obtained by means of PANalitical PW3050/60 X'Pert PRO MPD X-ray diffractometer with a Cu radiation (K_{α}=1.54060Å) and a Ni filter in Bragg-Brentano configuration, equipped with a X'cellerator detector. The diffractograms were acquired in the $5° \leq 2\theta \leq 70°$ range with an acquisition step of 0.01°.

XRD deconvolution of individual patterns was obtained in the 2 theta = 11-31° range using a multiple peak fit with pseudo-Voight functions to identify the individual component. Peak parameters, including FWHM, were determined for the main XRD reflections, as obtained from the X-ray diffraction profile fitting.

N_2 adsorption-desorption experiments were performed at 77 K by means of Micromeritics ASAP 2020 instrument (Micromeritics, Norcross, GA, USA) to investigate the porosity properties of the materials obtained via thermal polymerization of a mixture of urea and melamine with different mass ratios. Before analysis, the samples were outgassed overnight at 423K. The *surface area (S_{BET})* was calculated by the Brunauer–Emmett–Teller (BET) equation (in the relative pressure range of 0.15–0.25 p/p0). Total pore volume was obtained from the amount of N_2 adsorbed at the 0.97 p/p0. Micropore surface area and volume were calculated from N_2 adsorption isotherms using the Harkins and Jura t-plot equation. Mesopore surface area (S_{meso}) was calculated by subtracting the micropore surface area (S_{micro}) from the total surface area (S_{tot}). The pore size distributions (PSDs) were derived from the N_2 adsorption isotherms using a non-negative least square fitting on the adsorption isotherm data by applying the density functional theory (DFT) method (N_2-DFT model, slit geometry) by means of the MicroActive Datamaster 5.02 software (Micromeritics)

Raman measurements were performed by a Renishaw Raman Microscope 1000 instrumentation and a 785 nm exciting laser line (diode Renishaw laser). Laser light (with a final power at the sample of 0.06 mW) was focused through a 20x ultra-long-working-distance Olympus objective (NA = 0.4), so obtaining a final laser light power density of 0.03 mWm^{-2}. Each presented Raman spectrum has been obtained as the average of three spectra (each one corresponding to 20 acquisitions of 20”) recorded on 3 different points of the same sample. Back-scattered light has been collected through the same objective, analysed by means of a 1200 l/mm grating and recorded through a Peltier cooled NIR enhanced detector.

FTIR spectra were acquired by means of a Bruker VECTOR22 spectrometer equipped with a cryogenic MCT detector with 2 cm^{-1} resolution in transmission mode. Due to the high absorbance of the samples in the IR spectrum, the materials dilution inside KBr salt (2% by weight) was necessary. Each sample was pressed in the form of self-supporting pellet and then analyzed under dynamic vacuum at 298 K.

UV-visible spectra were obtained by means of Cary 5000 UV-vis-NIR spectrophotometer equipped with a diffuse reflectance sphere, in the diffuse reflectance

(DR) mode. Due to the strong absorption, the samples were diluted in polytetrafluoroethylene (PTFE) powder (about 2% of sample by weight) and the spectra were acquired in the 2500-190 nm wavelengths range after collecting PTFE powder 100% reflectance baseline used as a reference. The energy gap values have been computed by means of Tauc's plots.

Photoluminescence (PL) spectra have been obtained at RT using a 350 nm excitation light of a conventional Xe arc lamp (HORIBA Jobin Yvon Fluorolog-3 instrument). To minimize reflections of the incident light, the samples were placed at 15° from the specular direction.

The *thermal stability* of the samples obtained from pure urea, pure melamine and from 50:50 mass ratio was investigated by thermogravimetric (TG) analyses with a heating rate of 20°C/min up to 900 °C either under N_2 gas or under air flows (being the last one for samples obtained from pure precursors) by means of TAQ600 (TA Instruments, New Castle, USA) instrument.

2.3. Photocatalytic performances assessment

Each g-C_3N_4 based sample (5 mg) was dispersed via soft sonication in 10 ml of methylene blue (MB) water solution (12.5 mg L^{-1}) and kept 30 minutes under dark conditions at room temperature to equilibrate the systems. The concentration of MB in water can be assumed to be representative of a wastewater system. The light irradiation experiments were performed in air at atmospheric humidity conditions utilizing a SOL 2/500S lamp (Honle UV technology, Munchen, Germany). The lamp provided a solar-like spectrum covering a range from UV to IR radiation (approximately 295-3000 nm). The power density was around 450W/m2, which is comparable to the annual irradiance at the Equator. To control the temperature at 298±5 K and to prevent the MB thermal degradation, a homemade air fan system and a thermostatic bath were used during the light exposure. After irradiation, the sample dispersion was centrifuged at 8000 rpm for 15 min. Photocatalytic degradation of MB has been investigated using UV-vis spectroscopy (Cary 5000 UV-vis-NIR spectrophotometer) in the transmission mode. The intensity of the adsorbed MB manifestations (C) was used to obtain C/C_0 vs. time plots, where C_0 is the concentration, corresponding to the initial intensity before illumination.

Please, all figures should be in colour.

3. Results and discussion

A preliminary evaluation of the reaction yields was necessary to understand the observed mass differences between M-C_3N_4 and U-C_3N_4, (Table 1 and Figure S1). Interestingly, the reaction yield of M-C_3N_4 accounted for about 48% of the initial amount of melamine, while U-C_3N_4 showed a yield of about 4% of the initial amount of urea. Based on this, dual-precursor samples were prepared with progressively increased melamine percentage, to achieve higher reaction yields still keeping the peculiar U-C_3N_4 properties. As a matter of fact, the reaction yield is increasing with the melamine percentage, also considering all the synthetized samples including the 98:2 (U_{98}-C_3N_4) and the 90:10 (U_{90}-C_3N_4) ones, not discussed in this contribution, for sake of brevity (Y[%] in Table 1 and black line in Figure S1). Notice that, the computation of the expected U_{98}-, U_{90}-, U_{80}- and U_{50}-C_3N_4 reaction yields (Y_{comp}[%] in Table 1 and red line in Figure S1), gives significantly different values from the experimental ones (m[g] in Table 1 and black curve in Figure S1).

More specifically, the experimental values are higher than the expected ones, which suggests effective and synergic interactions between the pristine components, thus favouring the growth of g-C_3N_4/g-C_3N_4 end products (*vide infra*).

Table 1. Experimental and estimated values of the reaction yields, where, m_0[g] = initial amount of precursors, m[g] = obtained amount of samples, Y[%] = obtained percentage yield, m_{comp} [g] = expected amount of samples and Y_{comp} [%] = computed percentage yield.

Sample	m_0 [g]	m[g]	Y [%]	m_{comp} [g]	Y_{comp} [%]
U-C_3N_4	1.53	0.06	4	0.06	4
U_{98}- C_3N_4	1.50	0.10	7	0.08	5
U_{90}- C_3N_4	1.50	0.17	11	0.13	9
U_{80}- C_3N_4	1.50	0.29	19	0.19	13
U_{50}- C_3N_4	1.53	0.53	35	0.40	26
M- C_3N_4	1.47	0.71	48	0.71	48

Although, in general, higher yields can be found in the literature [61], the occurrence of incomplete reactions as well as the formation of by-products cannot be excluded under the adopted conditions. In order to give insight on the stability and on the structure/properties relationship of the synthetized materials, a detailed overview of the obtained results will be given in the following.

3.1 Thermogravimetric analyses

Thermogravimetric (TG) and first derivative thermogravimetric (DTG) analyses were performed to assess the thermal stability of the synthesized samples. TG and DTG curves of M-C_3N_4, U_{50}-C_3N_4, U_{80}-C_3N_4 and U-C_3N_4, treated under nitrogen flow, are illustrated in Figure 1 a-d.

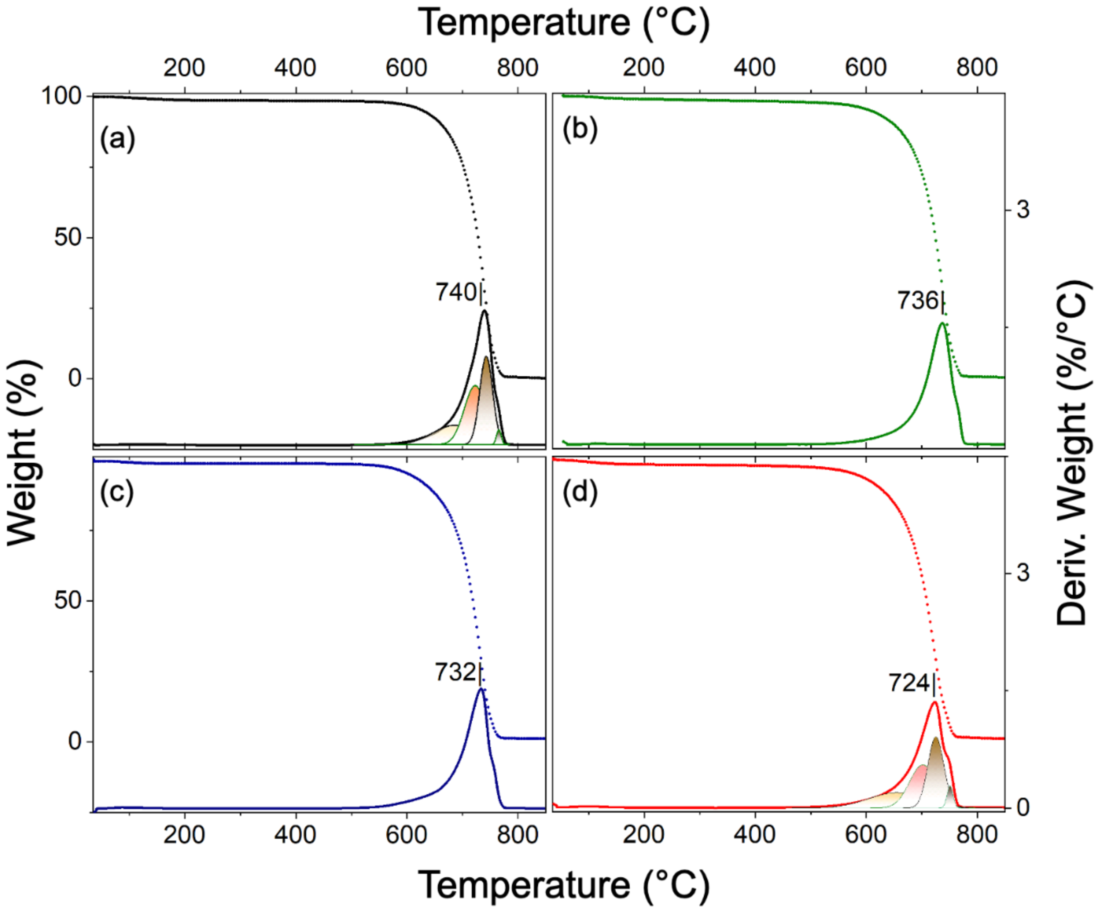

Figure 1. TG (dotted lines) and DTG (full lines) profiles of: M-C_3N_4 (a), U_{50}-C_3N_4 (b), U_{80}-C_3N_4 (c), and U-C_3N_4 (d) under N_2 gas flow. At the bottom of (a, d) deconvolution bands of the DTG signals are shown.

For all the samples a slight weight decrease (ca. 1.5 wt.%) attributed to physisorbed H_2O is observed at temperatures below ca. 200 °C, while the whole weight loss occurs in the 600-780°C range. Some more, it was found that the M-C_3N_4 exhibits higher thermal stability, as it decomposes completely at around 778 °C, whereas U-C_3N_4 is the least stable, with a decomposition temperature of 766°C. Notably, the behaviour of the mixed compositions (U_{50}-C_3N_4 and U_{80}-C_3N_4) falls between that of M-C_3N_4 and U-C_3N_4, as also confirmed by the observed shift in DTG peak maxima positions from 740 °C (M-C_3N_4) to 724°C (U-C_3N_4). A close analysis of the whole shape of the DTG curves, also considering the weak shoulder at slightly higher temperatures for all samples, reveals a complex decomposition process consisting of several overlapping transformations, as shown from the Gaussian deconvolution analysis (Figure 1 a, d). A detailed investigation of the obtained Gaussian curves is out of the scope of this contribution, however we can reasonably conclude that during the progressive degradation process different heptazine ring building units with different arrangements and thermal stabilities are developing. According to the discussed results, the following order of thermal stability: M-C_3N_4 > U_{50}-C_3N_4 > U_{80}-C_3N_4 > U-C_3N_4, can be ultimately confirmed.

For comparison, TGA of M-C_3N_4 and U-C_3N_4 has been carried out also under air flow (Figure S2 in SI). As expected, all the main exothermic peaks occur at a slightly lower temperature, thus demonstrating the high thermal stability of g-C_3N_4 also under an oxidizing atmosphere. From these results, it comes out that the obtained metal-free materials are highly stable and can be completely degraded without any residue.

3.2. Morphology by FESEM and AFM analyses.

The morphologies of the melamine and urea-derived g-C_3N_4 samples are SEM, FESEM and AFM imaged in Figures 2 a-e and 3 a-e. As previously discussed [20], the M-C_3N_4 shows complex and differently elongated aggregates, as well as large lamellar and hollow structures 5–15 μm in size, at the adopted resolution (Figure 2a).

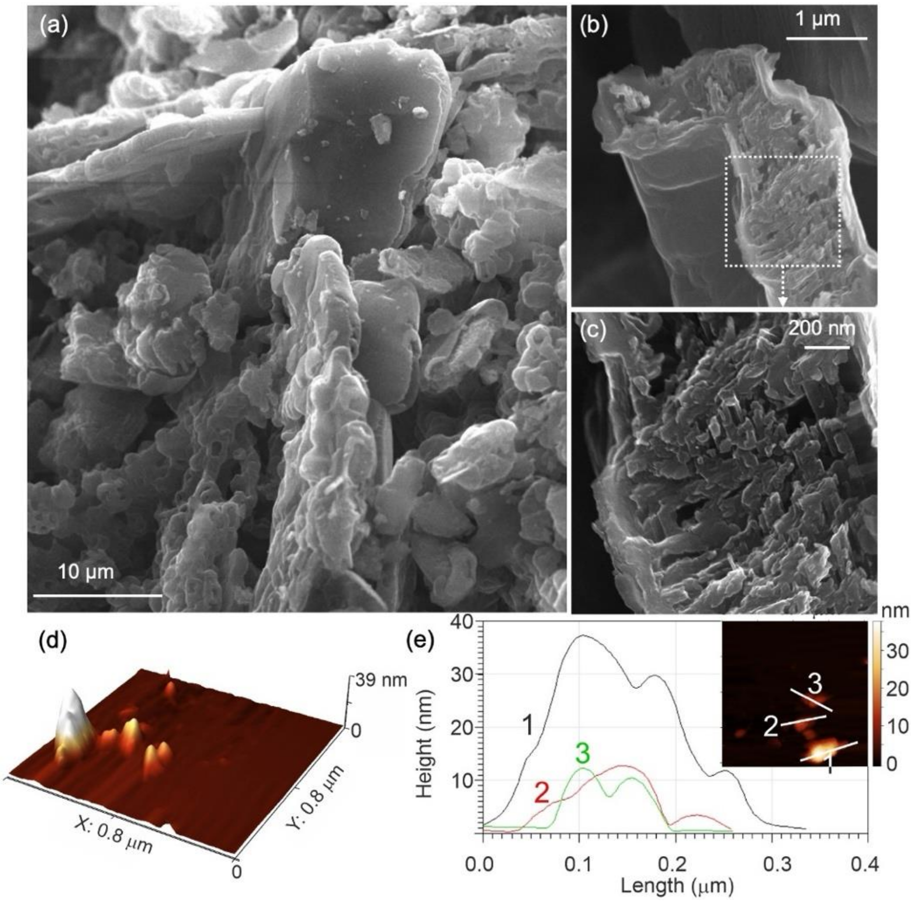

Figure 2. M-C_3N_4 FESEM images on different regions (a-b), enlarged view (c) of a selected area in (b). 3D AFM image (d) and AFM height profiles (e) along three selected lines, as shown in the inset therein.

The high level of aggregation due to the stacking of micron-sized lamellas is explained with sintering effects, which in turn reflects on the low surface area (*vide infra*). Detailed high resolution FESEM image (Figure 2b) and the enlarged view (c) on a selected area in (b) clearly highlight the dense arrangement made by a large amount of interconnecting lamellas. Further insight into the material's structure, that is into the compact aggregation state and the robust nature of the particle assembling, after sonication in solution, is revealed through AFM images (Figure 2d) and AFM height profiles (Figure 2e), along a few aggregates. More isolated 3D structures are observed on the flat freshly cleaved mica support, and the related complex profile envelope suggests the presence of differently sized aggregates, ranging from 10 to several tens of nanometers, still present even after sonication.

Conversely, the U-C_3N_4 sample exhibits a porous and open structure, which consists of thin curly nano-sheets, resulting in the formation of a large amount of micro/nanopores, in agreement with the high specific surface area (*vide infra*) (Figures 3a, b, c).

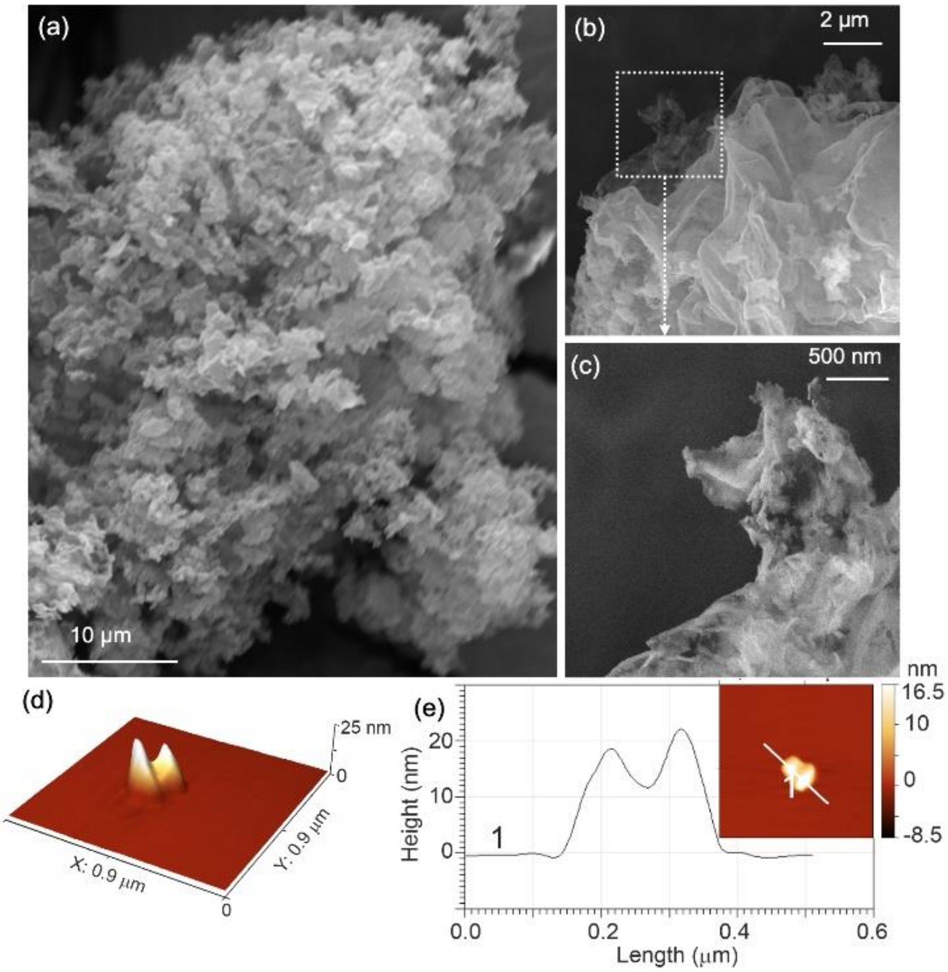

Figure 3. U-C_3N_4 FESEM images (a-b), exploded view (c) on the selected region in (b). 3D AFM image (d) and AFM height profile (e) along the selected line, as shown in the inset therein, of sample.

From the AFM image (Figure 3d) and the height profile (Figure 3e), the U-C_3N_4 particles appear to be arranged also into small aggregates 10-20 nm in size. Therefore, in both the melamine- and urea-derived g-C_3N_4 samples, the formation of more or less extensive aggregates, is confirmed, at the adopted resolution, whose vertical size can be estimated in the range of tens of nanometres. Notice that, the high degree of aggregation observed from FESEM and AFM analyses, prevents us from evaluating accurately the crystallite size, then from matching the scattering domain values, as obtained from XRD analysis *(vide infra)*.

According to some authors, the distinct morphology of M-C_3N_4 and U-C_3N_4 samples can be explained with the different condensation pathways [62]. In particular, during the thermal condensation of urea, the presence of oxygen causes the gas evolution of different compounds, *i.e.* H_2O, NH_3, CO_2 thus forming highly porous structures and a large amount of folded nanosheets, unlike the bulk-like structure of the M-C_3N_4, where mainly condensed g-C_3N_4 domains, embedded in a less condensed "melon-like" framework, have been thoroughly shown [20,63].

The morphologies of two melamine/urea derived g-C_3N_4 samples (*i.e.* 50:50 (U_{50}-C_3N_4) and 80:20 (U_{80}-C_3N_4) are also FESEM (Figures 4 a, b and Figures 5 a, b,) and AFM (Figures 4 c, d and Figures 5 c, d) imaged. For the 98:2 (U_{98}-C_3N_4) sample, see Figure S3 in Supporting Information).

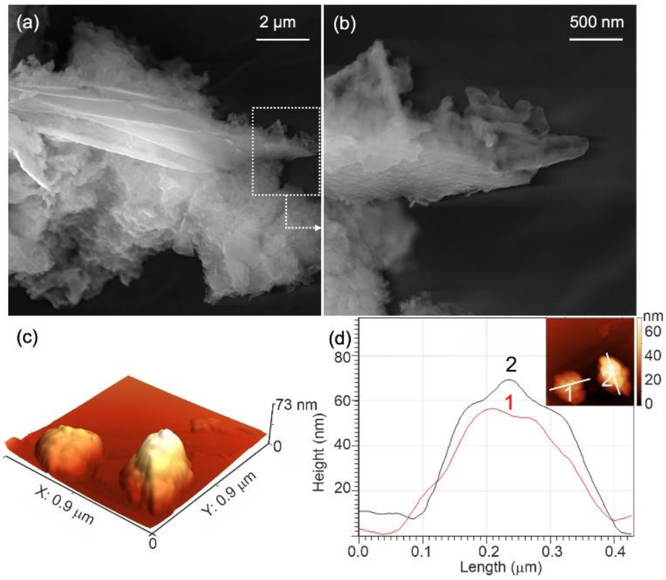

Figure 4. U_{50}-C_3N_4 FESEM image (a), exploded view (b) on the selected region in (a). 3D AFM image (c) and AFM height profiles (d) along two selected lines, as shown in the inset therein.

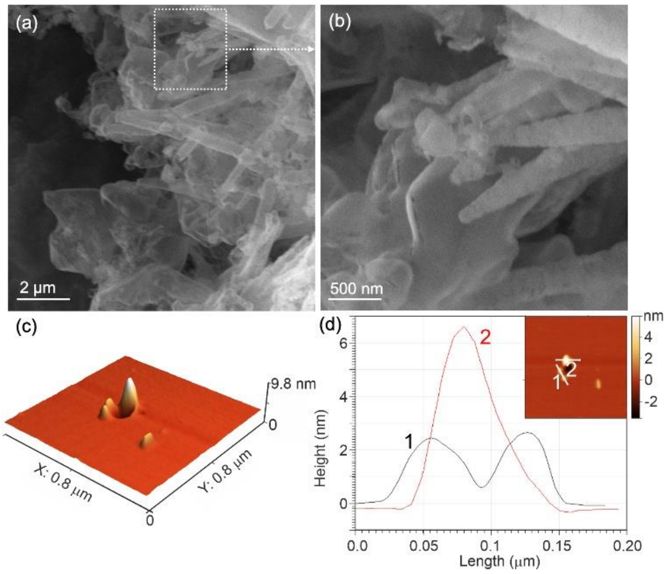

Figure 5. U_{80}-C_3N_4 FESEM image (a), exploded view (b) on the selected region in (b). 3D AFM image (c) and AFM height profiles (d) along two selected lines, as shown in the inset therein.

It is worthy of attention that, moving from U_{50}-C_3N_4, to U_{80}-C_3N_4, samples, the more stacked lamellar structures change into thinner and/or folded nanolayers inside a porous structure (Figures 4 a, b and 5 a, b). Hence, the porous structure becomes progressively predominant with the increase of the urea amount in the melamine/urea mass ratio. At the same time, the aggregation level, appear to decrease gradually from U_{50}-C_3N_4, to U_{80}-C_3N_4 and the formation of dense agglomerates due to the melamine precursor is mostly hindered. In fact, as aforementioned, the release of gaseous components due to the decomposition of urea co-precursor has a key role in forming highly porous structures. However, from a careful observation of FESEM images displayed in Figures

4 a, b and 5 a, b, it comes out that the U_{50}-C_3N_4, and U_{80}-C_3N_4, samples appear as a combination of M-C_3N_4 stacked layered structures, that are tightly enveloped by U-C_3N_4 thinner nano-sheets (U_{50}-C_3N_4 in Figure 4 a-b) or sandwiched between ultrathin coiled layers (U_{80}-C_3N_4 in Figure 5 a-b).

In figures 4c-d and 5c-d, portions of U_{50}-C_3N_4 and U_{80}-C_3N_4 surfaces are 3D-AFM imaged, that confirm the local formation of less aggregated nanostructures, also more isolated and progressively smaller in height moving from the U_{50}-C_3N_4 (Figure 4c) to the U_{80}-C_3N_4 (Figure 5c) sample. Actually, from the observed height profiles along different directions, (insets in Figures 4d, and 5d), the vertical sizes of the aggregated nanoparticles can be estimated in the range of ten and units of nanometres for U_{50}-C_3N_4 and U_{80}-C_3N_4 samples, respectively, though, in case of U_{80}-C_3N_4 samples, greater sizes cannot be excluded. This agrees with the highly heterogeneous nature of the U_{50}-C_3N_4 and U_{80}-C_3N_4 samples. It seems that, moving to either M-C_3N_4 and U-C_3N_4 samples, the related height profiles increase. Conversely, samples obtained from a mixture of both precursors show less dense networks, which leads to a consequent easier fragmentation, also compared to U-C_3N_4 sample.

From a more in-depth analysis of U_{80}-C_3N_4 sample, as shown by high-resolution FESEM images, (Figures 6a-c), an extensive porous and apparently flexible network, made by curly thin and small layers, has been well highlighted.

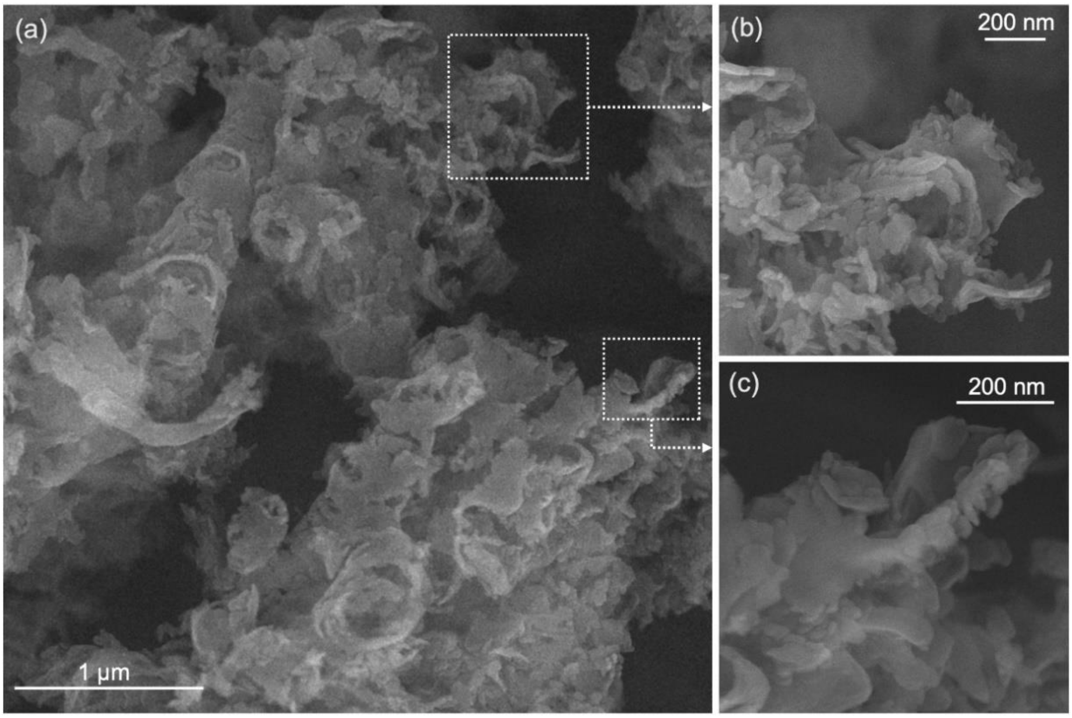

Figure 6. U_{80}-C_3N_4 FESEM image (a), exploded views (b-c) on the selected regions in (a).

This consists of a variety of mesopores, at the adopted resolution, which could give rise to good permeability and conceivably to a plethora of different nano-scale interfaces. Notice that, from N_2 adsorption-desorption isotherms (*vide infra*), that were carried out on the as-prepared samples, the average pore size and pore volume values will be provided with higher accuracy and will be compared with the preliminary indications obtained by FESEM investigations.

3.3. Structure by TEM, SAED, XRD and HRTEM analyses

3.3.1. TEM and SAED analyses

From a more careful analysis of the evolution of the nanocrystalline structures, as a function of the melamine/urea mass ratio, BF-TEM images and SAED patterns were acquired on all the samples (Figure 7a-d). Moving from M-C_3N_4, U_{50}-C_3N_4, U_{80}-C_3N_4 up to U-C_3N_4, the morphology is remarkably changing from the bulkier flakes of M-C_3N_4 to the thinner and crinkled layers of U-C_3N_4 sample, in agreement with the previously described FESEM images.

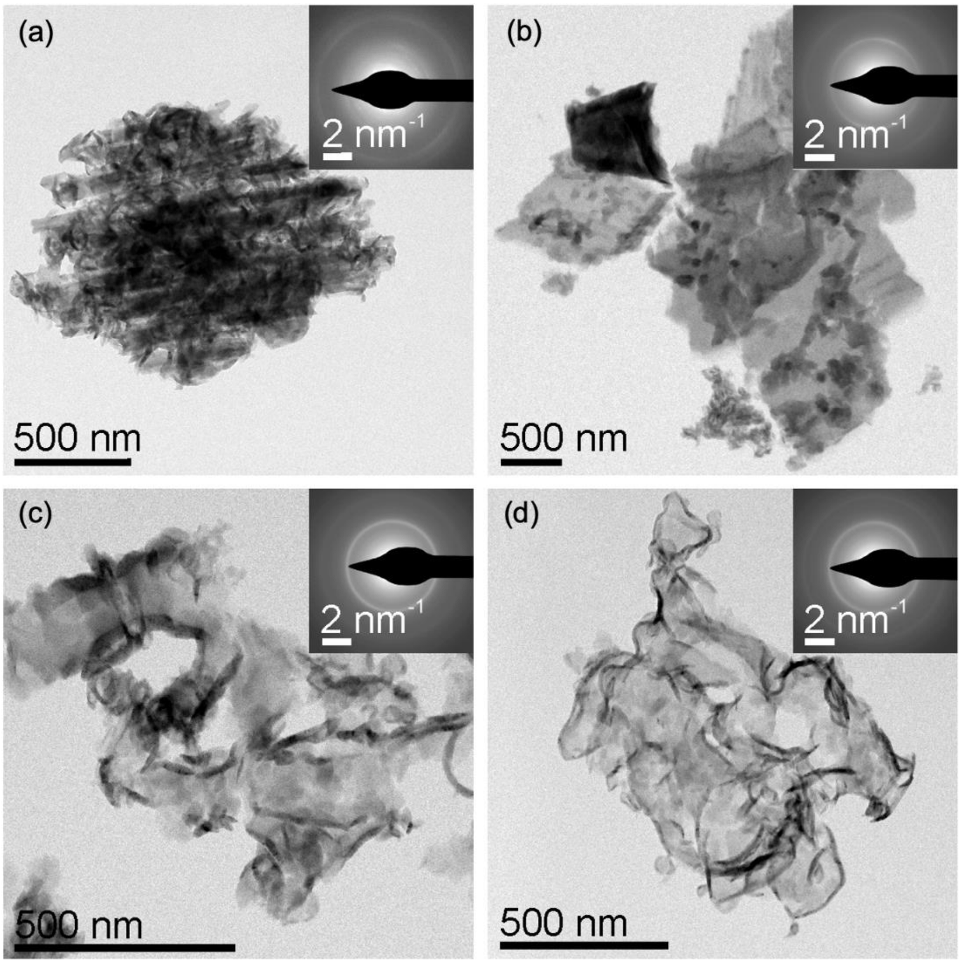

Figure 7. BF-TEM images of M-C_3N_4 (a), U_{50}- C_3N_4 (b), U_{80}- C_3N_4 (c), and U-C_3N_4 (d) with corresponding SAED patterns in the insets.

In SAED patterns (insets in Figure 7a-d), all the samples show diffraction rings on a diffuse background, suggesting a material composed of nanometer-sized domains. The highest intensity rings occur at spacings of 6.8 Å and 3.2 Å: the first spacing is due to the in-plane packing of heptazine units, and it could be assigned to the (210) diffraction planes of an orthorhombic unit cell, while the second spacing is due to the (002) planes, *i.e.* the inter-layer $\pi - \pi$ stacking in the slightly hydrogenated g-C_3N_4 structure reported previously (ICSD 194747) [20,64-68]. In particular, slightly stretched and enlarged spots on weak diffraction rings are observed for M-C_3N_4 sample, which is indicative of the preferred orientation of larger crystalline domains. Moving to urea containing samples, the ring corresponding to (002) planes of g-C_3N_4, due to the crinkled and rolled-up thin foils with the extended face parallel to (001) planes of the structure, turns to become more intense.

These spacings are consistent with the diffraction peaks observed in the XRD patterns of the samples *(vide infra)*.

3.3.2. XRD patterns

The XRD patterns of all samples are shown in Figure 8. Notably, two main peaks are observed for each sample: 2θ ≈13.1° and 2θ≈27.4° for M-C_3N_4, 2θ≈13.0° and 2θ≈27.6° for U_{50}-C_3N_4, 2θ≈13.0° and 2θ≈27.6° for U_{80}-C_3N_4, 2θ≈12.8° and 2θ≈27.5° for U-C_3N_4. The XRD features are consistent with layered g-C_3N_4 systems, according to literature data [64-69]. The intense XRD peak at 2θ ≈ 27° (002 crystal planes), corresponding to a distance d(002) ≈ 3.2 Å, is attributed to the inter-layer $\pi - \pi$ stacking [20,64,65], as before discussed from SAED pattern.

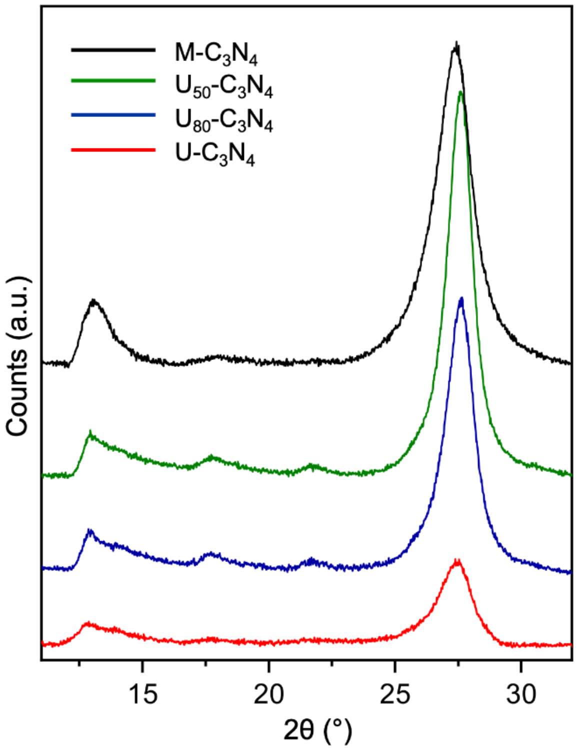

Figure 8. XRD patterns of the synthetized samples: U-C_3N_4 (red line), U_{80}- C_3N_4 (blue line), U_{50}- C_3N_4 (green line) and M-C_3N_4 (black line).

Notice that, a small shift of (002) reflection toward higher 2θ values for U_{80}-C_3N_4 and U_{50}-C_3N_4 samples can be highlighted, which reflects on a decreasing of interlayer distance.

The feature at 2θ ≈ 13°, corresponding to a distance d(210) ≈ 6.8Å, is due to the in-plane packing of heptazine units, and is assigned to the (210) diffraction planes of an orthorhombic unit cell, as before shown from SAED pattern [20,64-68].

Notably, all the XRD patterns show broad and weak reflections at approximately $2\theta \approx 18°$ and $2\theta \approx 22°$, which are due to the residual presence of hydrogen-bonded triazine/heptazine units inside the framework [20].

Furthermore, from the computed integrated intensity ratios between the $2\theta \approx 27°$ and $2\theta \approx 13°$ diffractions peaks for the M-C_3N_4 and U-C_3N_4 samples, higher values were obtained in case of M-C_3N_4, which can be attributed to the higher level of aggregation of M-C_3N_4, already observed from FESEM images, and to the preferential orientation of the extended (002) face parallel to the support (Figure S4 and Table S1) [62,70]. Notice that a high polymerization degree could be shown also from FTIR results *(vide infra).* Conversely a lower intensity for the peak at about 27° would indicate a lower level of aggregation with the presence of thinner foils, as obtained for U-C_3N_4. Hence, we can state that the ratio between the $2\theta \approx 27°$ and $2\theta \approx 13°$ diffraction peaks could provide information on the aggregation level, hence on the morphology of each sample. Some more, from XRD patterns, the domain sizes can also be obtained. Regard to this, the coherently scattering domain sizes (D_{hkl}) were calculated from the Scherrer's equation: $D_{hkl} = k\lambda/\beta\cos\theta$, where λ is the X-ray wavelength, β is the FWHM of the diffraction line corrected by the instrumental broadening, θ is the diffraction angle, and K is the Scherrer's constant or shape constant, which could be assumed to be 0.9, in agreement with Alizadeh *et al.*[71].

In particular, from the $2\theta \approx 13°$ and from $2\theta \approx 27°$ diffraction peaks, the in-plane coherence lengths ($D_{//}$ *i.e.* D_{210}) and the out-of-plane coherence lengths ($D_\perp$ *i.e.* D_{002}) respectively, were estimated for all the samples (Table 2).

Table 2: Diffraction peaks of (210) and (002) planes with the corresponding in-plane coherence lengths ($D_{//}$), out-of-plane ($D_\perp$) and shape anisotropy from ($D_{//}/D_\perp$) ratio.

Sample	2θ° (210)	$D_{//}$ (nm)	2θ° (002)	$D_\perp$ (nm)	$D_{//}/D_\perp$
M-C_3N_4	13.1	8.6	27.4	**5.1**	**1.7**
U_{50}-C_3N_4	13.0	9.6	27.6	**7.3**	**1.3**
U_{80}-C_3N_4	13.0	16.3	27.6	**7.2**	**2.5**
U-C_3N_4	12.8	9.0	27.5	**5.3**	**1.7**

According to some authors [72,73], the coherence scattering lengths were defined as approximately 1/FWHM for the $2\theta \approx 27°$ and for $2\theta \approx 13°$ diffraction peaks (Table 2), which enables the size of the crystallite domains to estimate, along perpendicular and parallel directions with respect to the layers in the orthorhombic g-C_3N_4 phase. Concerning this, the increase of coherence length was related to higher degrees of crystalline perfection, on the contrary, a lower coherent length results in more disordered crystalline samples [73]. Additionally the shape anisotropy, defined as the ratio between the domains dimensions along parallel and orthogonal directions ($D_{//}/D_{\perp}$) [72], can also been obtained (Table 2).

As for the $D_{//}$ and $D_{\perp}$ scattering domains given in Table 2, quite similar values are obtained for M-C_3N_4 and U-C_3N_4, although slightly higher for U-C_3N_4.

This means that the peak broadening would be determined not only by the crystallite finite size, but also by a variety of factors including dislocations, stacking faults, twinning, *etc.* These are responsible of higher FWHM values, which would lead to lower coherence scattering length (Figure 8 and Figure S4). Since these factors are not considered, the coherence scattering domains are larger than those predicted by Scherrer equation, in particular for more defective urea-derived samples.

Concerning the U_{50}-C_3N_4, and more remarkably the U_{80}-C_3N_4 mixtures, higher coherence scattering lengths, respect to U-C_3N_4 and M-C_3N_4 are obtained, thus suggesting remarkably higher intra-layer and inter-layer crystalline orders for both the materials made from the different precursors. Also, a peculiar shape anisotropy can be obtained for U_{80}-C_3N_4 sample, as shown by the higher coherence length along (210) planes, whereas values closer to M-C_3N_4 and U-C_3N_4 are shown for U_{50}-C_3N_4 sample, probably due to the relevant role played by the high proportion of melamine precursor.

The evident discrepancy between the FESEM, AFM results and the scattering domains obtained from XRD analysis, can be reasonably explained with the high level of aggregation, due to restacking phenomena, which results in the formation of networks, though with different level of porosity.

3.3.3. HRTEM and FFT images

Beside TEM and SAED analyses, HRTEM images combined with fast-Fourier Transforms (FFTs) of melamine and urea-derived g-C_3N_4 samples (Figures 9-12) give detailed structural information, concerning mainly interlayer spacing and orientation spread, thus providing a local view of the crystal structure of the material.

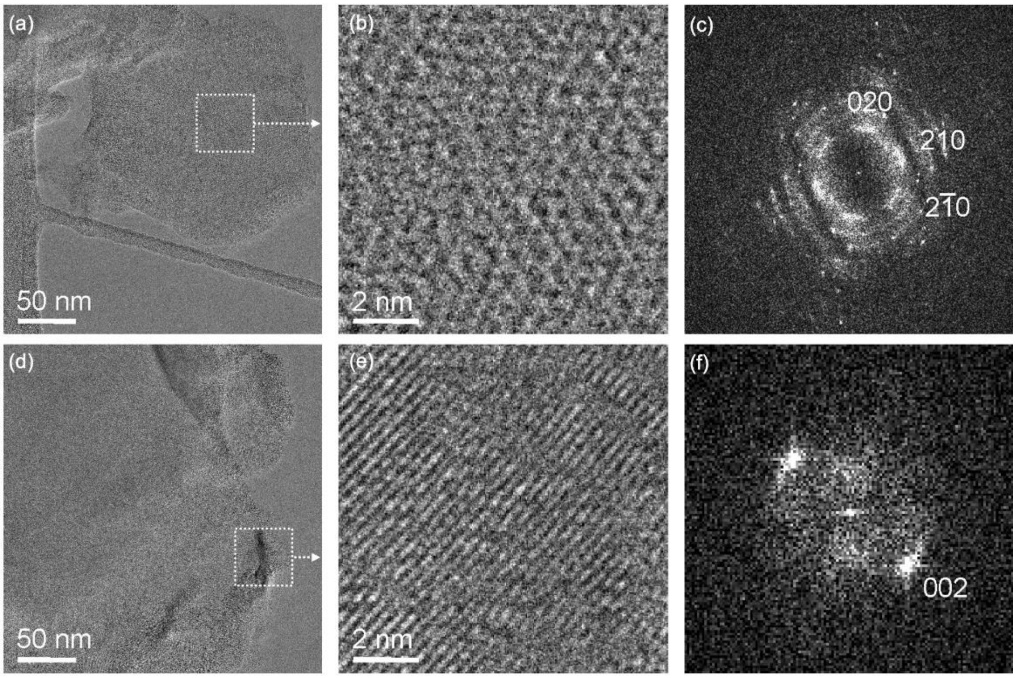

Figure 9. M-C_3N_4 HRTEM images (a, d) with the enlarged views (b, e) and the corresponding FFTs (c, f) on (b) and (e) regions respectively. The indexing refers to the structure ICSD 194747.

In particular, in Figures 9a-c, a M-C_3N_4 flat area (a), with an enlarged view (b) of a selected region in (a) are HRTEM imaged with the corresponding FFT pattern (c). The magnified HRTEM image and the corresponding FFT are compatible with [001] orientation (Figure 9b-c). The bright arcs are assigned to the (210) and (020) diffraction planes of the in-plane packing of heptazine units within an orthorhombic symmetry. The arc shape of (210) and (020) reflections proves the in-plane twist due to misalignment of the heptazine strands, *i.e.* the strands are not perfectly aligned, which would result in regular spots on the FFT.

Beside flat areas, on M-C_3N_4 sample many folded regions can also be highlighted in Figure 9d. The magnified HRTEM image a selected region in (d) and the corresponding FFT pattern (Figures 9e-f), show well-defined fringes and intense diffraction spots, respectively, associated with (002) planes due to the inter-layer $\pi - \pi$ stacking of the orthorhombic symmetry.

Moving to U_{50}-C_3N_4 sample, from HRTEM image of a flat region (Figure 10a) and from the enlarged view of a selected area therein (Figure 10b), fringes corresponding to (002) crystalline planes are also observed. The FFT (Figure 10c) on a selected area in Figure 10a shows a twisted distribution of spots corresponding to (210) planes, which means that crystallites have random orientation within the selected area.

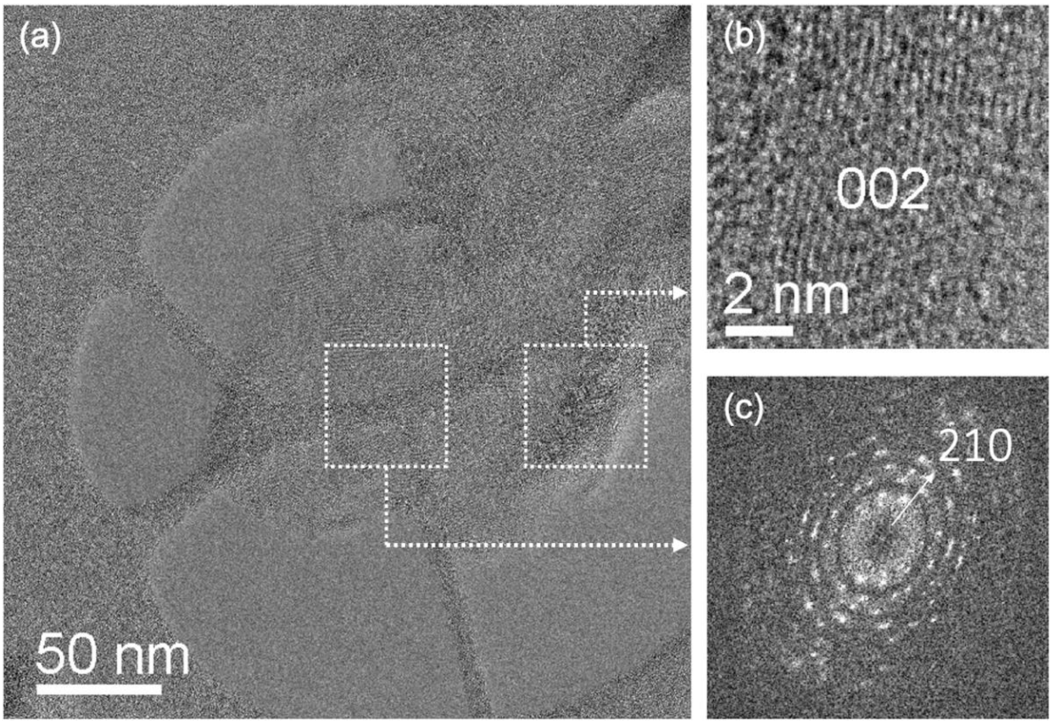

Figure 10. U_{50}-C_3N_4 HRTEM image (a) with enlarged view (b) and FFT (c) of the two selected regions. The indexing refers to the structure ICSD 194747.

From HRTEM images of the U_{80}-C_3N_4 sample, regions corresponding to (002) planes, at different magnification, can be highlighted (Figure 11a-b). A selected area in correspondence of a folded flake in Figure 11a is HRTEM imaged in Figure 11b, where fringes corresponding to (002) crystalline planes are also observed. Considering the FFT image of the selected flat area (Figure 11c), rings and bright spots are mainly observed, due to the (210) diffraction planes, which means the crystallites orientations become even more random distributed than in the above-discussed samples.

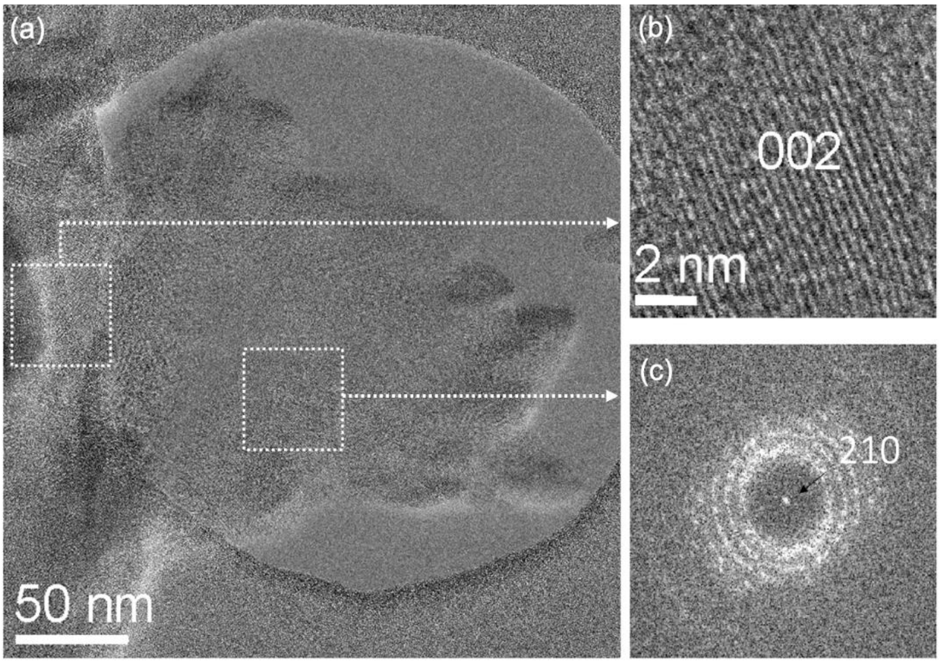

Figure 11. U_{80}-C_3N_4 HRTEM image (a) with enlarged view (b) and FFT (c) of the two selected regions. The indexing refers to the structure ICSD 194747.

Lastly, regions of the U-C_3N_4 sample are HRTEM imaged in Figures 12 a-e. More in detail, from Figure 12a an extended and heterogeneous area with the simultaneous presence of flat and folded flakes can be highlighted. Moving to the magnified HRTEM image of a flat area (Figure 12b) and to the corresponding FFT (Figure 12c), the prevailing presence of rings, typical of randomly oriented crystallites, confirms the disordered nature of the U-C_3N_4 sample.

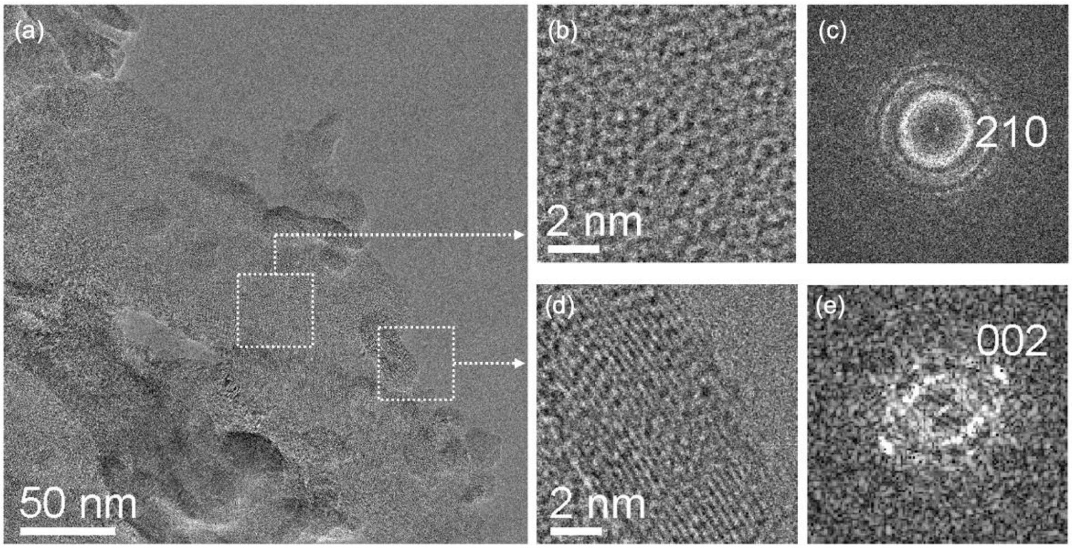

Figure 12. U-C_3N_4 HRTEM image (a) with enlarged views on two areas (b, d) and FFT patterns (c, e) of two selected regions. The indexing refers to the structure ICSD 194747.

It is noteworthy, that the edges of the flakes are also folded (Figure 12a), hence from the high resolution image and FFT pattern shown in Figure 12d and Figure 12e, respectively, the (002) planes are obtained.

In conclusion, HRTEM analyses highlight the evolution from bulky crystals to randomly oriented polycrystalline systems, when going from M-C_3N_4 to U-C_3N_4 samples, via intermediate situations shown by U_{50}-C_3N_4 and U_{80}-C_3N_4.

In summary, HRTEM confirms the results obtained by XRD and SAED analyses and allows to identify at a local level the arrangement of nanocrystalline domains within the g-C_3N_4 fragments.

3.4. N_2 adsorption/desorption isotherms, pore size distributions.

The 77K N_2 adsorption/desorption isotherms and the pore size distributions of all samples, are shown in Figures 13 a-b, while their porosity properties are summarized in Table 3.

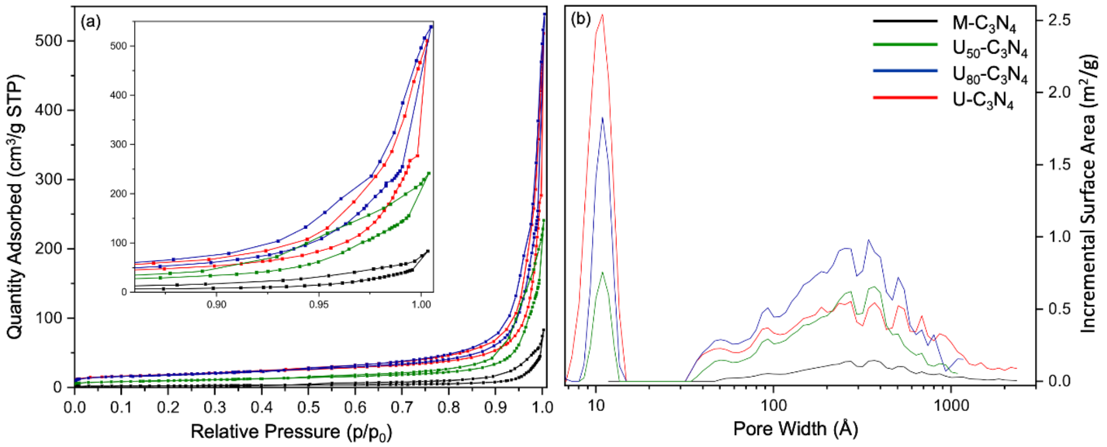

Figure 13. 77K N_2 adsorption−desorption isotherms (a), corresponding pore size distributions (b) in terms of incremental surface area of: U-C_3N_4 (red line), U_{80}-C_3N_4 (blue line), U_{50}-C_3N_4 (green line) and M-C_3N_4 (black line).

Table 3: BET surface area (S_{tot}), micropore (S_{micro}) and mesopore (S_{meso}) surface areas.

Sample	S_{tot} (BET) [m^2/g]	S_{micro} [m^2/g]	S_{meso} [m^2/g]
M-C_3N_4	8.6	0.7	7.9
U_{50}-C_3N_4	34.8	2.7	32.1
U_{80}-C_3N_4	64.8	6.3	58.5
U-C_3N_4	64.4	11.3	53.0

The isotherms of the four samples are of type IV (BDDT Classification) [74] with the hysteresis loops shape of a H3 type, which could suggest the formation of slit-shaped pores, thus indicating the main mesoporous character of the samples (Figure 13 a) [74]. Considering the hysteresis loops in Figure 13a, a shift to lower pressure values with increasing urea content is observed, thus reflecting on the higher surface area values of the corresponding samples. More in detail, also by comparing the results reported in Table 3, for U-C_3N_4, U_{80}-C_3N_4, U_{50}-C_3N_4 and M-C_3N_4, the BET surface area is progressively decreasing, with the aggregation level, as expected. This has been explained with the release of CO_2 during the condensation pathways in urea-derived C_3N_4 samples, which is responsible of higher surface area, thus suppressing the advance of grain boundary [52]. As for the porosity results, a wide family of meso/macropores in the 30–1000 Å range is shown for all the samples, together with the additional contribution of small micropores lower than 15 Å in size, (Figure 13b). Namely, from the results of the incremental surface area (Figure 13b), significant differences concerning the pore size distribution can be highlighted, when melamine derived g-C_3N_4 and urea derived g-C_3N_4 samples are compared. In particular, M-C_3N_4 mainly shows meso/macroporous structures, whereas the U-C_3N_4 surface area is due to a contribution of either micro- or mesoporosity. For this reason, the higher amount of urea content within the mixed systems (i.e. U_{50}-C_3N_4, U_{80}-C_3N_4) results, as expected, in the increasing of the microporosity of the samples (Figure 13b and Table 3). However, when considering the mesopores region (in the 20Å - 500Å size range), beside the M-C_3N_4 low incremental surface area, due to the high level of aggregation of stacked micron-sized lamellas, a higher incremental surface area is observed for U_{80}-C_3N_4 as compared to that of U-C_3N_4. This means that the presence of a specific amount of melamine (20% by weight) inside the urea powder could promote the formation of larger voids, thus increasing the mesoporosity of the final sample.

Indeed, as confirmed from FESEM images, U_{80}-C_3N_4 consists mainly of thin layers located either on the exterior surface or inside of bulkier C_3N_4 domains, whose stacking is mostly hindered, thus enhancing, in both cases, the whole mesoporosity.

Notice that, beside the BET surface area, also the pore structure could play a crucial role in affecting any catalytic activity.

3.5. Vibrational properties by Raman investigations

Raman spectra of the g-C_3N_4 samples, acquired with 785 nm laser line, are reported in Figure 14 a,b. Wide and extended features are obtained, although overshadowed by an extensive fluorescence background (Figure 14a). Identifying the single Raman features is quite difficult

(Figure 14a), however after background removal, the typical g-C_3N_4 features *i.e.* at 1236 cm^{-1}, 1215 cm^{-1} , 980 cm^{-1} , 770 cm^{-1} and 707 cm^{-1} in all samples can be easily identified, which agrees reasonably well with the many data reported in literature [75-78] (Figure 14b).

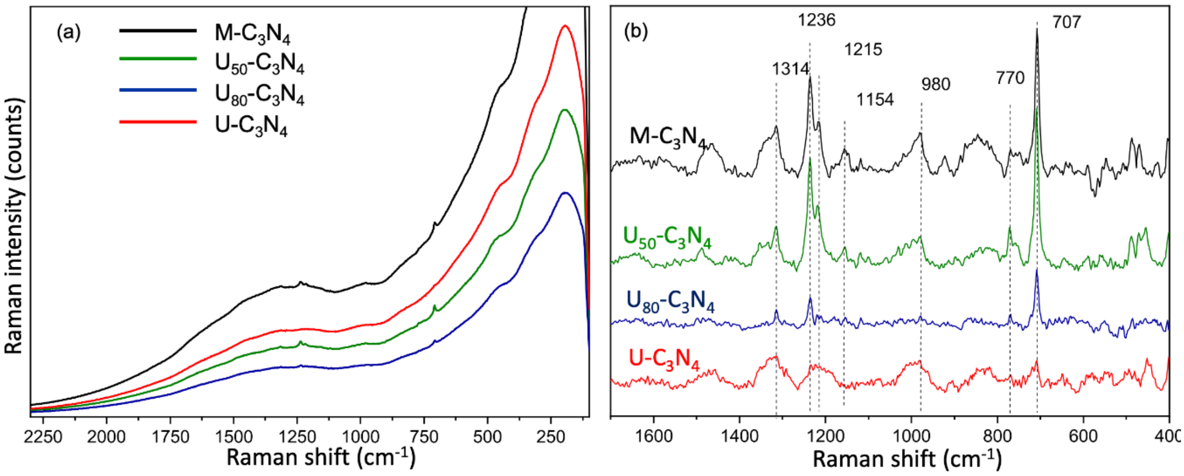

Figure 14. Raman spectra recorded with 785 nm excitation laser before (a) and after (b) background subtraction: M-C_3N_4 (black line), U_{50}-C_3N_4 (green line), U_{80}-C_3N_4 (blue line), and U-C_3N_4 (red line)

The feature centered at about 1236 cm^{-1}, together with the 1215 cm^{-1} shoulder, can be assigned to the typical stretching vibration modes of C=N and C-N bonds inside the heterocycles and usually they are related to the presence of defects and/or disorder in the graphite-like structure [66,79] . The weak peaks at 1154 and 770 cm^{-1}, clearly visible in M-, U_{50}- and U_{80}-C_3N_4, (Figure 14b) are both assigned to the A_1' vibrations of tri-s-triazine (heptazine) rings [76] or, according to other authors [66], to E' semi-circle stretching vibrations together with the NH_2 rocking mode. Notice that, the strong 707 cm^{-1} feature is also assigned to A_1' vibrations of heptazine rings breathing modes [66].

Based on literature data [77], the 770 cm^{-1} and 707 cm^{-1} couple of peaks are due to layer-layer deformation vibrations, being the I_{770}/I_{707} intensity ratio also indicative of the layer stacking amount. In particular, a small intensity ratio is typical of a bulk system, while the ideal 1-layer g-C_3N_4 shows a I_{770}/I_{707} of about one. Concerning our samples, the increased urea precursor content leads to a decreased I_{770}/I_{707} ratio, hence a lower amount of stacked layers may be expected, in agreement with morphology (see FESEM and HRTEM images) and BET surface area measurements. Indeed, this peculiar behavior can also affect the electronic properties, thus causing quantum confinement effects and, consequently, higher energy gap for samples with higher urea content *(vide infra)*.

The broad feature centered at 980 cm^{-1} is assigned to the s-triazine ring breathing mode of residual melamine species [76,80], which means that a complete transformation has not been obtained, in agreement with FTIR results (*vide infra*). It is known that, the 980 cm^{-1} feature has been assigned to different graphitic phases and polymorphs of g-C_3N_4, which means that it can be currently considered as an index of condensation level in g-C_3N_4 based systems [75,81]. By this time, to perform a more detailed assignment of Raman spectra of the different g-C_3N_4 systems, a periodic quantum-mechanical investigation at the Density Functional Theory level (DFT), by means of the periodic simulation code CRYSTAL23 [82] was performed. More in detail, according to our previous work, the simultaneous presence of a few condensed g-C_3N_4 domains embedded in a less condensed "melon-like" framework has been shown [20].

In this regard, we adopted the model proposed by Fina *et al.* based on their XRD and neutron diffraction analyses [64]. The computational set up (Paragraph S5) and computed Raman spectrum (Figure S5) are reported in Supplementary Information, for sake of brevity.

However from the careful analysis of the experimental Raman features (Figure 14b), compared to the computed ones (Figure S5), three main regions can be easily identified: (i) 3500 cm^{-1} - 3000 cm^{-1} region, due to NH_2 and NH terminal groups, (ii) 1800 cm^{-1} - 900 cm^{-1} region, due to in-plane heptazine rings deformations, (iii) 900 cm^{-1} - 600 cm^{-1} region, due to out-of-plane heptazine rings deformations. In particular, a detailed assignment can be found in Table S2, from which a well agreement with the experimental results can be shown.

Notice that, the 980 cm^{-1} feature is absent on the computed Raman spectra, because the isolated triazine rings are not present in the model [Figure S5].

In conclusion, we can state that the Raman features clearly account for the different level of layer stacking in samples obtained from different M and U precursor mass ratios, moving from bulkier flakes (*i.e.* M-C_3N_4) to porous and less dense networks (*i.e.* U-C_3N_4).

3.6. Vibrational properties by FTIR spectra

The FTIR spectra of the as-prepared samples are compared in Figure 15. From a detailed analysis of FTIR spectra previously obtained from melamine [20,22,81,83], the accurate assignment of all the features has been carried out. In general, quite similar absorptions in the main three regions (*i.e.* 3000-3500 cm^{-1}, 1750-1100 cm^{-1} and 900-700 cm^{-1}) can be actually identified for all g-C_3N_4 samples, thus confirming similar lattice modes [62,84].

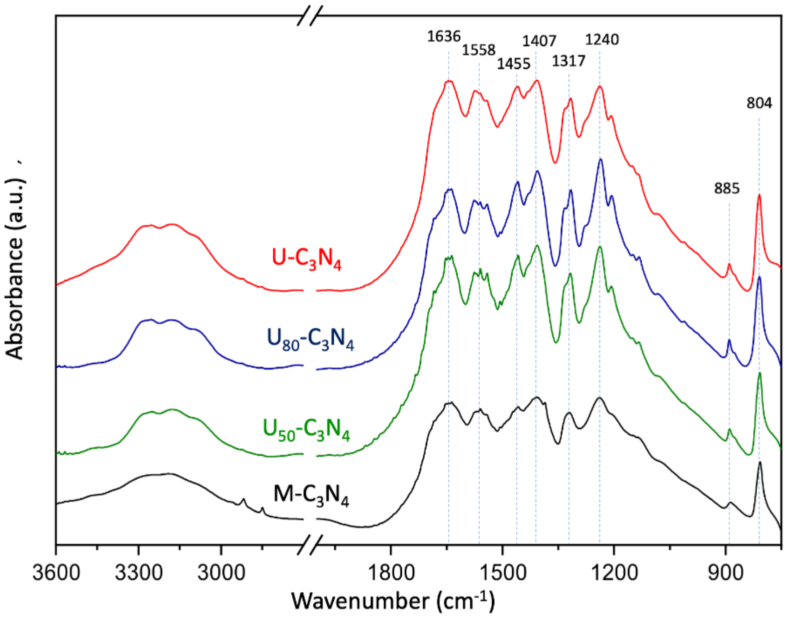

Figure 15. FTIR spectra of M-C_3N_4 (black line), U_{50}-C_3N_4 (green line), U_{80}-C_3N_4 (blue line), and U-C_3N_4 (red line).

More specifically, the broad absorption in the 3500–3000 cm^{-1} range has been assigned to the combination of symmetric and asymmetric stretching modes of NH/NH_2 terminal groups, of a melon-like structure, while the broadening is explained with H-bonding interactions [65-67,85-91]. Some more, wide absorptions in the 1750-1100 cm^{-1} range, due to the typical fingerprint of C-N and C=N stretching modes of N-containing heterocycles [88-91] can be recognized in all samples together with the sharp peaks in the 900-700 cm^{-1} range due to the breathing mode/out-of-plane bending vibration of the heptazine units [65,67,86,88]. Triazine unit and N-H bending vibrations are identified by maxima at 804 and 885 cm^{-1}, respectively.

Notice that, moving along the sequence of spectra from M-C_3N_4 (black line in Figure 15) to U-C_3N_4 (red line in Figure 15), the integrated area ratios between the (3500–3000 cm^{-1}) and (1750–1100 cm^{-1}) main regions are increasing, which can be explained with a plausible higher amount of the terminal units (NH_2). The detailed values of the integrated area are reported for sake of completeness in Table S3. Namely, this provides a further indication that many defective situations, including amino groups, were introduced within the urea derived g-C_3N_4 frameworks, precisely because of the urea thermal polymerization process.

Lastly all the observed features are confirming the occurrence of complex structures with different level of defectivity, consisting of condensed g-C_3N_4 domains embedded in less condensed frameworks [20].

3.7. Optical properties, energy gap (UV-vis, Tauc plots) and Photoluminescience properties.

The optical properties of the g-C_3N_4 samples, obtained from the different precursors, were investigated by means of UV-Vis spectroscopy. The UV-visible spectra together with the computed Tauc's plots for the indirect band gap estimations, typical of bulk systems, are shown in Figure 16 and insert therein. From Figure 16, the sharp absorption edge of g-C_3N_4, due to the transition from HOMO N^{3-} $2p_{x,z}$ antibonding orbitals to the LUMO N^{3-} $2p_z$ and C^{4+} $2p_{x,z}$ lowest energy orbitals, can be recognized in all samples [21].

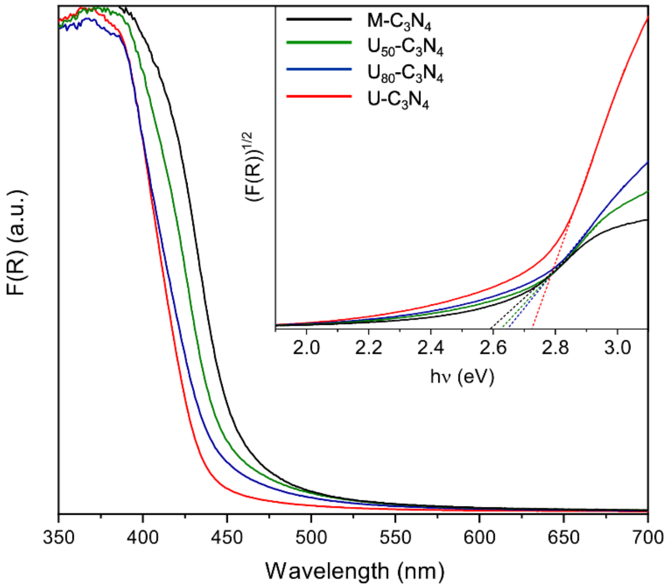

Figure 16. UV-Vis spectra and computed Tauc's plots for band gap estimations (Inset) of M-C_3N_4 (black line), U_{50}-C_3N_4 (green line), U_{80}-C_3N_4 (blue line) and U-C_3N_4 (red line).

A significant blue shift towards shorter wavelengths from melamine to urea derived samples can be highlighted, as result of quantum size effects (Figure 16). More in details, from the evaluation of the optical band gap, the extrapolated onsets, estimated by the Tauc's plots (insert in Figure 16), give an indirect band gap values of 2.72 eV and 2.59 eV for samples obtained from urea and melamine single precursor, respectively, which are in good agreement with the values reported in literature [20,65,67,83,87,92-94]. The observed blue shift of the absorption edge, already ascribed to the quantum confinement effect [84], can be reasonably explained with the reduced stacking of the g-C$_3$N$_4$ nanosheets due to the gas release during the thermal polycondensation of urea [55] (*vide* Raman analysis). As expected, the absorption edges of the samples obtained from mixed precursors, are in between the before mentioned energy gaps and the values are increasing with the urea content. In particular, values of 2.66 eV and 2.63 eV have been obtained from U$_{80}$-C$_3$N$_4$ and U$_{50}$-C$_3$N$_4$ Tauc's plot estimations, respectively.

To shed light on the photoluminescence properties of the as-prepared samples, absorption spectra were acquired, under the 350 nm excitation. The obtained PL spectra exhibit a broad and intense emission peak at ~460-465 nm, that is almost the same for all synthetized g-C$_3$N$_4$ based samples (black, green, blue and red lines in Figure 17 a-d). These features can be explained, in general, with electron-hole recombination phenomena (scheme in Figure 17e).

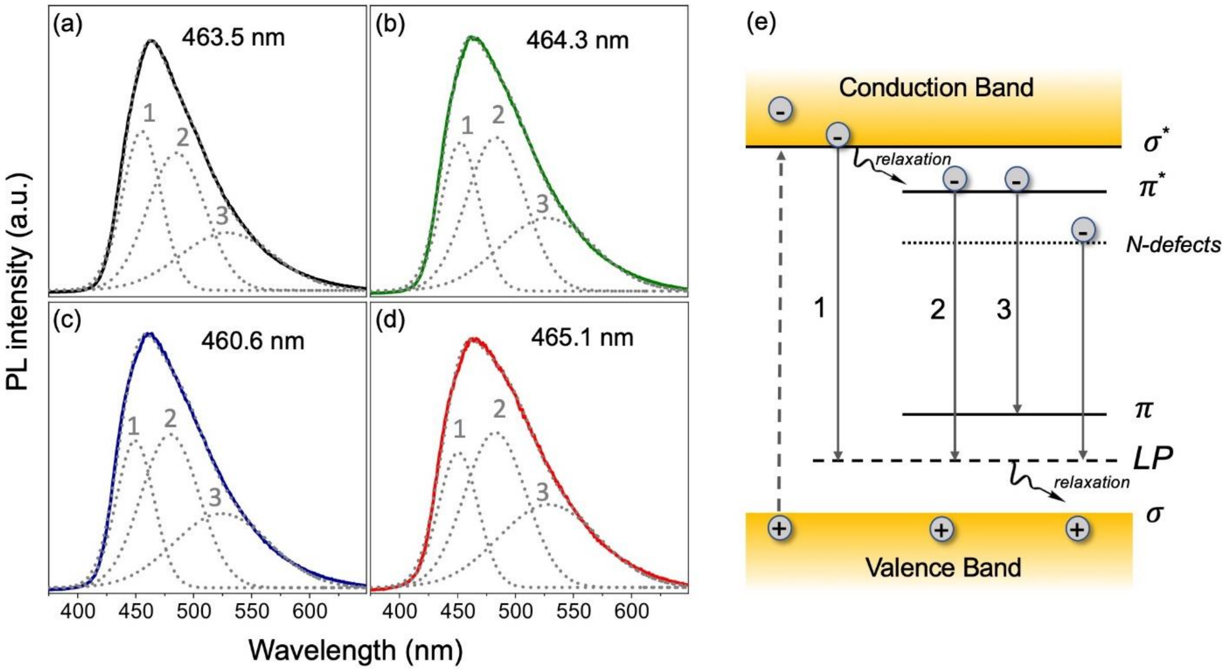

Figure 17: PL emission spectra, of M-C_3N_4 (a), U_{50}-C_3N_4 (b), U_{80}-C_3N_4 (c) and U-C_3N_4 (d), samples using 350 nm excitation light. Gaussian fitting: cumulative peak fit and deconvolution components (labelled as 1, 2 and 3) of PL emission spectra are shown by dotted curves. (e) Scheme of emission transitions. The dashed vertical arrow shows excitation transition while the 1, 2, 3 continue arrows show radiative emission transitions. The curled arrows represent non-radiative relaxation transitions.

The broad and asymmetric character of the emission bands, that are well fitted by grey dotted lines, means many recombination processes via specific energy levels are simultaneously contributing to the light emission, maybe even predominant over the fundamental σ^* - σ band-to-band recombination (scheme in Figure 17e) [95,96].

From a careful comparison of the emission spectra (Figure 17a-d), the frequency values of the PL maxima red-shift slightly with the urea precursor content, from ~ 463.5 to ~465.1 nm, except for U_{80}-C_3N_4, whose emission is blue shifted at ~ 460.3 nm (Table S4).

We may assume that the recombination of photogenerated charges is less favored in U_{80}-C_3N_4 as compared to U-, U_{50}- and M-C_3N_4. This can be explained with the porous structure of U_{80}-C_3N_4 , which affects both the light absorption efficiency either the charge separation efficiency, thus reducing the electron –hole recombination rate. Moving from M-C_3N_4 (Figure 17a) to U-C_3N_4 (Figure 17d), a progressively increased FWHM (full widths at half-maximum) value (from 76 nm to 95 nm) can also be calculated. This is indicative of the increased surface area with higher amount of structural defects for urea containing samples, which in turn causes many emission levels to contribute within the energy gap. *(vide infra).*

From the PL spectra deconvolution obtained by means of a detailed Gaussian fitting (Figure 17a-d), three main components: (1) in the 450-456 nm, (2) 480-486 nm and (3) 524-529 nm intervals, can be highlighted with average full widths at half-maximum (FWHM) of about 33 nm, 51 nm, and 82 nm, respectively (Table S4).

Based on this and on the scheme (Figure 17e), three main transition pathways can be highlighted, *i.e.* the $\sigma^* \rightarrow$ LP (Lone Pair) level at 450-456 nm, $\pi^* \rightarrow$LP level at 480-486 nm and $\pi^* \rightarrow \pi$ transitions at 524-529 nm, respectively [66,97,98], the last one typical for all π-conjugated carbon-based materials [97-99].

As reported by Chubenko *et al.* [95,96], a relation between the g-C_3N_4 polymerization degree and the intensity ratio of 1 and 2 luminescence features has been found. In fact, when the polycondensation reaction proceeds, it is known more heptazine units form chemical π-bonds with each other, thus causing the prevailing of (2) $\pi^* \rightarrow$LP level emission transitions.

Concerning our g-C_3N_4 specimens, obtained from progressively increased amount of urea precursor, the observed higher intensity of the (2) component with respect to the (1) one, could be indicative of the higher polymerization, that is the higher coherence lengths inside the (210) planes (*see XRD results*) of the more extended, even if highly defective, thin layers.

As it is well known, the luminescence properties of the carbon nitride materials are considered mainly affected by the presence of the sp^2 C-N clusters, that form a π-conjugated polymeric network, and by the lone-pair electrons of nitride, beside states consisting of sp^3 C-N σ band. According to some authors [95,96], the valence band is made by C-N σ-bonds with sp^3 hybridization (σ levels), C-N π-bonds with sp^2 hybridization (π levels) and LP levels of nitrogen, while the conduction band is made by σ^* and π^* levels. Due to their close position, excited electrons at the σ^* levels relax to π^* levels, thus providing channels for the charge delocalization. Hence, a more detailed discussion, beyond our study, should take into account that a plethora of phenomena, including radiative emissions from σ^* and/or from π^* to the valence band and to nitrogen lone pair levels, from nitrogen defect levels inside the forbidden gap (*i.e* C≡N triple bonds, NH_2 groups, vacancies) to valence band and to nitrogen LP levels have to be considered, the last ones shown in scheme (Figure 17e).

3.8. Methylene blue photodegradation tests

The photocatalytic activity of the all the systems was evaluated, by investigating the MB degradation in acqueous solution under solar-light irradiation, covering approximately the 295-3000 nm range. The absorption spectra *(not reported for sake of brevity)* for the MB photo-degradation have been used to obtain C/C_0 vs. time plots, where C_0 is the concentration, corresponding to the initial intensity before illumination.

Figure 18 (a, b) shows the relationship between C/C_0 vs. photodegradation time and the obtained apparent rate constants of the different photocatalysts, respectively. Furthermore, 0-, 1- and 2-kinetic order plots were fitted and their goodness of fit, represented by R^2 values, was calculated (Supplementary Materials, Table S5). Based on the R^2 values, we can assume that the Langmuir-Hinshelwood first-order kinetic model [100] ($\ln C_0/C = k$, where k is the apparent first-order constant) fits well our experimental results with photocatalysts, while the MB photodegradation with no photocatalyst is better described by a 0-order kinetic reaction, as commonly found in dye degradation [101]. Notice that, after 30 minutes of equilibration procedure under dark conditions, the samples (i.e., U-C_3N_4, U_{80}-C_3N_4, U_{50}-C_3N_4 and M-C_3N_4) show different adsorption percentages towards MB. In particular, the adsorbed amounts are about 1%, 2%, 10% and 8% respect to the initial MB concentrations, for M-C_3N_4, U_{50}-C_3N_4, U_{80}-C_3N_4 and U-C_3N_4, respectively.

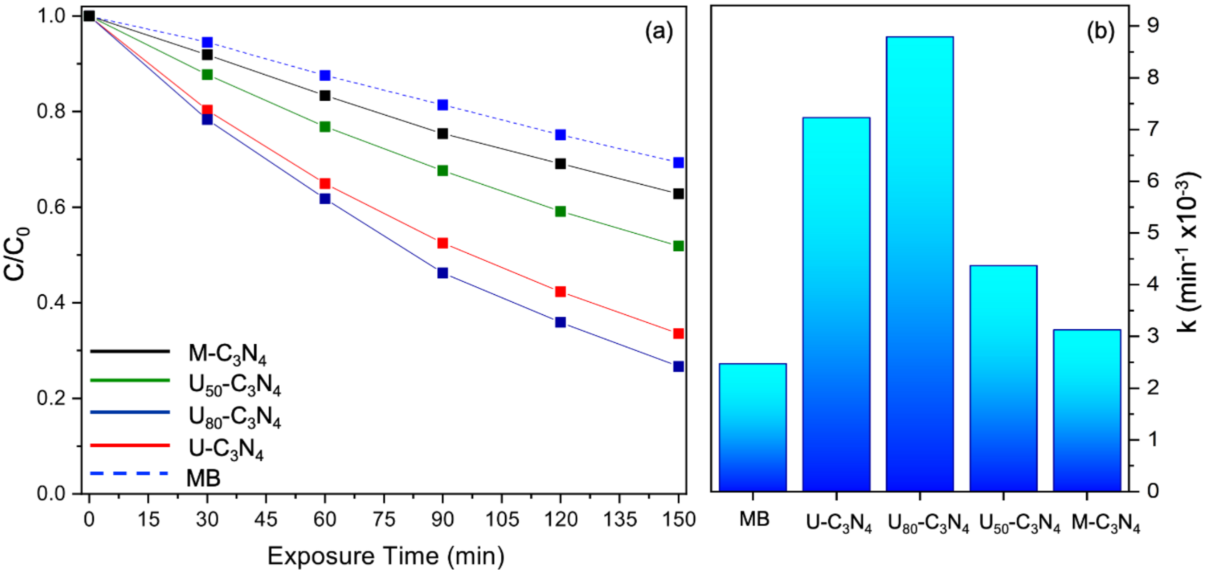

Figure 18. (a) MB Photodegradation efficiencies as function of time, (b) apparent rate constants of U-C_3N_4, U_{80}-C_3N_4, U_{50}-C_3N_4 and M-C_3N_4.

In general, during the whole irradiating time, the best photodegradation performances have been observed for samples obtained from precursors with higher urea contents, i.e. U-C_3N_4, U_{80}-C_3N_4, in agreement with the higher surface area values from BET measurements. As a matter of fact, the degradation rates are in the following order: M-C_3N_4 < U_{50}-C_3N_4 < U-C_3N_4 < U_{80}-C_3N_4. Notice that a nonlinear behaviour among U_{80}-C_3N_4 and U-C_3N_4 must be highlighted, being the highest photodegradation efficiency surprisingly observed for U_{80}-C_3N_4, as also reported Niu et al. [55] even if towards RhB photodegradation.

Many factors can be considered to explain the peculiar high photodegradation efficiency of U_{80}-C_3N_4, including the greatly improved surface area with respect to the other systems, which, implies an increased amount of active sites, the highest $D_{//}/D_{\perp}$ coherent lengths ratio, *i.e.* the highest shape anisotropy associated with a large in-plane correlation length with a resulting turbostratic crystalline disorder [72] and also the lower inter-planar distance that allows to reduce the charge transport distance from the bulk to the surface of material [102]. Therefore, after sonication treatments for short time, that are the prerequisite for the subsequent photodegradation reaction and for AFM investigations, a few layered, highly porous nanocrystals can be easily obtained, as observed in case of U_{80}-C_3N_4 network. Concerning this point, the reader is reminded of the U_{80}-C_3N_4 AFM images, that prove a relevant reduction of the aggregate's sizes, after sonication processes. Based on these results, we can hypothesize that extensive contacts among different g-C_3N_4 nanostructures, made from urea/melamine 80:20 mass ratio, provide a suitable surface area together with many nanochannels inside the porous network, thus favouring charge transfer between the two components and establishing feasibly close contacts among different g-C_3N_4.

4. Conclusions

In this study, g-C_3N_4 based-materials were synthesized via thermal polycondensation of different melamine/urea mass ratios as starting precursors, aiming to give some insight on the role of urea/melamine ratio on the structure/properties relationship of g-C_3N_4/g-C_3N_4 nanoarchitectures. As well imaged from FESEM/AFM, the stacked micron-sized lamellas of M-C_3N_4 change into the porous and open structures consisting of small sized domains of U-C_3N_4. From HRTEM imaging, a direct visualization of the bulky-flake nature of M-C_3N_4, as compared to the thinner and more randomly oriented thin layers of U-C_3N_4 was also provided, in agreement with XRD data, which gives information on interlayer distances and on in-plane heptazine packing.

Concerning the $D_{\perp}$ and $D_{//}$ coherence lengths, as estimated from XRD patterns, the U_{50}-C_3N_4, and more remarkably the U_{80}-C_3N_4 mixtures show higher coherence scattering lengths, respect to U-C_3N_4 and M-C_3N_4, thus suggesting a peculiar higher intra-layer crystalline order for both the materials made from the different precursors.

HRTEM analyses also provide a local crystallographic view of such evolution, *i.e.* from bulkier crystal flakes to randomly-oriented thin curly nano-sheets, when going from M-C_3N_4 to U-C_3N_4 samples, via intermediate situations shown by U_{50}-C_3N_4 and U_{80}-C_3N_4. This is confirmed by adsorption/desorption isotherms and pore size distributions, *i.e.* the BET surface area is progressively increasing, with the increased microporosity and polycrystalline nature, moving from M-C_3N_4 to U-C_3N_4.

The enhanced content of urea from M-C_3N_4 to U-C_3N_4 samples reflects also on Raman features, also supported by quantum mechanical calculations (Raman).

Additionally, FTIR and Raman spectroscopic features, highlight an increased defectivity due to the NH and NH_2 terminal groups (FTIR) together with a low stacking level moving from M-C_3N_4 to U-C_3N_4 samples (Raman), in agreement with FESEM and HRTEM images. Further evidence of the role of urea in promoting in-plane formation of extended, even if highly defective, thin layers, comes from the accurate analysis of PL spectra.

The U_{80}-C_3N_4 samples are particularly challenging due to their peculiar properties with respect to the other systems, which makes it attractive to many fields, including photocatalysis.

Indeed, the U_{80}-C_3N_4 structure, with its higher energy gap, could also explain quantum confinement effects typical of few-layered materials.

Some more, besides the high thermal stability (TGA) and significant reaction yields, due to melamine action, U_{80}-C_3N_4 shows also improved surface area, extensive porous network, which implies an increased number of active sites and a lower inter-planar distance due to urea action. This could reflect on extensive contacts among different g-C_3N_4 domains, thus establishing more effective interfaces, which favour the charge transfers between the two components. Based on all these factors, the peculiar high photodegradation efficiency towards MB degradation of the few layered, highly porous U_{80}-C_3N_4 network, must be highlighted, also surprisingly superior to that of U-C_3N_4.

On the basis of the results discussed so far, we can definitely state that a realistic model, able to explain the experimental results, implies the combination of different structural motifs, including the prevailing formation of bulkier flakes for M-C_3N_4 made by strands of highly condensed monomers, and thinner/coiled layers for U-C_3N_4, which gives rise to less dense networks, *i.e.* more porous and defective structures.

We point out that this study may give a further contribution to the knowledge of g-C_3N_4 based-materials, obtained from sustainable and/or recycled precursors, through simple synthesis methods. The role of the different melamine/urea precursors mass ratios on the structure/properties relationship was in-depth discussed, by means of a wide variety of characterization techniques.

Supplementary materials: Paragraph S1. Reaction yields (Figure S1: experimental and estimated reaction yields. Paragraph S2. Thermogravimetric analysis (Figure S2: Thermogravimetric analysis of M-C_3N_4 and U-C_3N_4 performed in air flux). Paragraph S3. Morphology of U_{98}-C_3N_4 (Figure S3: 3D AFM image and FESEM images of U_{98}-C_3N_4 sample). Paragraph S4: XRD powder diffraction (Figure S4: XRD powder diffraction pattern of M-C_3N_4 and U-C_3N_4; Table S1: XRD powder diffraction integrated area $I_{(210)}$ and $I_{(002)}$ of M-C_3N_4 and U-C_3N_4). Paragraph S5. Computed Raman spectrum (computational set up; Figure S5: Computed Raman spectrum of Melon structure; Table S2: Experimental and computed Raman vibrational modes with relative description). Paragraph S6. FTIR intensity ratio (Table S3: FTIR integrated area I^a and I^b on the 3600-2800 cm^{-1} and 1900-750 cm^{-1} main regions). Paragraph S7. Photoluminescence (Table S4: PL emission spectra and Gaussian deconvolution parameters of all samples). Paragraph S8. Methylene Blue photodegradation test (Table S5: Goodness of fit of photodegradation kinetic)

Author Contributions

P.N., F.C., A.D., R.B. and D.S. wrote and organized the manuscript; P.N., F.C., A.D., R.B and D.S. performed experiments and characterisations. In particular, P.N. and D.S. performed the sample preparation; P.N. performed FTIR, UV-Vis, surface area analyses and computational characterization; F.C. and P.N. performed TGA, XRD, AFM, FESEM, PL analyses and methylene blue photodegradation test; A.D. performed Raman analyses; R.B.

performed TEM and HR-TEM analyses; D.S. supervised the manuscript. All authors have read and agreed to the published version of the manuscript.

Conflicts of interest

There are no conflicts to declare.

Acknowledgements

The authors acknowledge support from CH4.0 under MUR (Ministero dell'Università e della Ricerca) for the university program "Dipartimento di Eccellenza 2023–2027", INSTM Consorzio, and the NIS (Nanomaterial for Industry and Sustainability) Inter-Departmental Center of University of Torino. The authors thank the Laboratory of the Chemistry Department and, in particular, Valsania, M. C., and Rebba E. for their support in FESEM acquisitions and Prof.ssa Silvia Maria Casassa for her precious support in the computational characterizations.

Notes and references

1. Novoselov, K.S.; Mishchenko, A.; Carvalho, A.; Castro Neto, A.H. 2D materials and van der Waals heterostructures. *Science (New York, N.Y.)* **2016**, *353*, aac9439-aac9439, doi:10.1126/science.aac9439.
2. Muscuso, L.; Cravanzola, S.; Cesano, F.; Scarano, D.; Zecchina, A. Optical, Vibrational, and Structural Properties of MoS2 Nanoparticles Obtained by Exfoliation and Fragmentation via Ultrasound Cavitation in Isopropyl Alcohol. *The Journal of Physical Chemistry C* **2015**, *119*, 3791-3801, doi:10.1021/jp511973k.
3. Tang, Q.; Zhou, Z. Graphene-analogous low-dimensional materials. *Progress in Materials Science* **2013**, *58*, 1244-1315, doi:https://doi.org/10.1016/j.pmatsci.2013.04.003.
4. Wang, F.; Pei, K.; Li, Y.; Li, H.; Zhai, T. 2D Homojunctions for Electronics and Optoelectronics. *Advanced Materials* **2021**, *33*, 2005303, doi:https://doi.org/10.1002/adma.202005303.
5. Mehmood, R.; Ahmad, Z.; Hussain, M.B.; Athar, M.; Akbar, G.; Ajmal, Z.; Iqbal, S.; Razaq, R.; Ali, M.A.; Qayum, A.; et al. 2D–2D heterostructure g-C3N4-based materials for photocatalytic H2 evolution: Progress and perspectives. *Frontiers in Chemistry* **2022**, *10*, doi:10.3389/fchem.2022.1063288.
6. Cravanzola, S.; Cesano, F.; Magnacca, G.; Zecchina, A.; Scarano, D. Designing rGO/MoS2 hybrid nanostructures for photocatalytic applications. *RSC Advances* **2016**, *6*, 59001-59008, doi:10.1039/C6RA08633K.
7. Santalucia, R.; Negro, P.; Vacca, T.; Pellegrino, F.; Damin, A.; Cesano, F.; Scarano, D. In Situ Assembly of Well-Defined MoS2 Slabs on Shape-Tailored Anatase TiO2 Nanostructures: Heterojunctions Role in Phenol Photodegradation. *Catalysts* **2022**, *12*, doi:10.3390/catal12111414.
8. Chaves, A.; Azadani, J.G.; Alsalman, H.; da Costa, D.R.; Frisenda, R.; Chaves, A.J.; Song, S.H.; Kim, Y.D.; He, D.; Zhou, J.; et al. Bandgap engineering of two-dimensional semiconductor materials. *npj 2D Materials and Applications* **2020**, *4*, 29, doi:10.1038/s41699-020-00162-4.
9. Mino, L.; Cesano, F.; Scarano, D.; Spoto, G.; Martra, G. Molecules and heterostructures at TiO2 surface: the cases of H2O, CO2, and organic and inorganic sensitizers. *Research on Chemical Intermediates* **2019**, *45*, 5801-5829, doi:10.1007/s11164-019-04003-y.
10. Wang, J.; Wang, S. A critical review on graphitic carbon nitride (g-C3N4)-based materials: Preparation, modification and environmental application. *Coordination Chemistry Reviews* **2022**, *453*, 214338, doi:https://doi.org/10.1016/j.ccr.2021.214338.
11. Miller, T.S.; Jorge, A.B.; Suter, T.M.; Sella, A.; Corà, F.; McMillan, P.F. Carbon nitrides: synthesis and characterization of a new class of functional materials. *Physical Chemistry Chemical Physics* **2017**, *19*, 15613-15638, doi:10.1039/C7CP02711G.

12. Ismael, M. A review on graphitic carbon nitride (g-C3N4) based nanocomposites: Synthesis, categories, and their application in photocatalysis. *Journal of Alloys and Compounds* **2020**, *846*, 156446-156446, doi:10.1016/j.jallcom.2020.156446.
13. Safaei, J.; Mohamed, N.A.; Mohamad Noh, M.F.; Soh, M.F.; Ludin, N.A.; Ibrahim, M.A.; Roslam Wan Isahak, W.N.; Mat Teridi, M.A. Graphitic carbon nitride (g-C3N4) electrodes for energy conversion and storage: A review on photoelectrochemical water splitting, solar cells and supercapacitors. *Journal of Materials Chemistry A* **2018**, *6*, 22346-22380, doi:10.1039/c8ta08001a.
14. Rhimi, B.; Wang, C.; Bahnemann, D.W. Latest progress in g-C3N4 based heterojunctions for hydrogen production via photocatalytic water splitting: A mini review. *JPhys Energy* **2020**, *2*, doi:10.1088/2515-7655/abb782.
15. Hayat, A.; Sohail, M.; Ali Shah Syed, J.; Al-Sehemi, A.G.; Mohammed, M.H.; Al-Ghamdi, A.A.; Taha, T.A.; Salem AlSalem, H.; Alenad, A.M.; Amin, M.A.; et al. Recent Advancement of the Current Aspects of g-C3N4 for its Photocatalytic Applications in Sustainable Energy System. *Chemical Record* **2022**, *202100310*, doi:10.1002/tcr.202100310.
16. Wang, Y.; Wang, X.; Antonietti, M. Polymeric Graphitic Carbon Nitride as a Heterogeneous Organocatalyst: From Photochemistry to Multipurpose Catalysis to Sustainable Chemistry. *Angewandte Chemie International Edition* **2012**, *51*, 68-89, doi:https://doi.org/10.1002/anie.201101182.
17. Wang, X.; Maeda, K.; Thomas, A.; Takanabe, K.; Xin, G.; Carlsson, J.M.; Domen, K.; Antonietti, M. A metal-free polymeric photocatalyst for hydrogen production from water under visible light. *Nature Materials* **2009**, *8*, 76-80, doi:10.1038/nmat2317.
18. Liu, G.; Wang, T.; Zhang, H.; Meng, X.; Hao, D.; Chang, K.; Li, P.; Kako, T.; Ye, J. Nature-Inspired Environmental "Phosphorylation" Boosts Photocatalytic H2 Production over Carbon Nitride Nanosheets under Visible-Light Irradiation. *Angewandte Chemie (International ed. in English)* **2015**, *54*, 13561-13565, doi:10.1002/anie.201505802.
19. Wen, F.; Huang, X.; Li, Y.; Pang, L.; Xu, Y.; Zhang, T. Photocatalytic Synthesis of Ammonia from Pinecone Graphite-Phase Carbon Nitride Loaded with MoS2 Nanosheets as Co-catalysts. *Langmuir* **2023**, *39*, 8475-8483, doi:10.1021/acs.langmuir.3c00763.
20. Negro, P.; Cesano, F.; Casassa, S.; Scarano, D. Combined DFT-D3 Computational and Experimental Studies on g-C3N4: New Insight into Structure, Optical, and Vibrational Properties. *Materials* **2023**, *16*, doi:10.3390/ma16103644.
21. Akhundi, A.; Zaker Moshfegh, A.; Habibi-Yangjeh, A.; Sillanpää, M. Simultaneous Dual-Functional Photocatalysis by g-C3N4-Based Nanostructures. *ACS ES&T Engineering* **2022**, *2*, 564-585, doi:10.1021/acsestengg.1c00346.
22. Im, C.; Kirchhoff, B.; Krivtsov, I.; Mitoraj, D.; Beranek, R.; Jacob, T. Structure and Optical Properties of Polymeric Carbon Nitrides from Atomistic Simulations. *Chemistry of Materials* **2023**, *35*, 1547-1559, doi:10.1021/acs.chemmater.2c02843.
23. Jiang, L.; Yuan, X.; Pan, Y.; Liang, J.; Zeng, G.; Wu, Z.; Wang, H. Doping of graphitic carbon nitride for photocatalysis: A review. *Applied Catalysis B: Environmental* **2017**, *217*, 388-406, doi:https://doi.org/10.1016/j.apcatb.2017.06.003.
24. Suyana, P.; Ganguly, P.; Nair, B.N.; Pillai, S.C.; Hareesh, U.S. Structural and compositional tuning in g-C3N4 based systems for photocatalytic antibiotic degradation. *Chemical Engineering Journal Advances* **2021**, *8*, 100148-100148, doi:https://doi.org/10.1016/j.ceja.2021.100148.
25. Wen, J.; Xie, J.; Chen, X.; Li, X. A review on g-C 3 N 4 -based photocatalysts. *Applied Surface Science* **2017**, *391*, 72-123, doi:10.1016/j.apsusc.2016.07.030.
26. Zheng, Y.; Lin, L.; Wang, B.; Wang, X. Graphitic Carbon Nitride Polymers toward Sustainable Photoredox Catalysis. *Angewandte Chemie - International Edition* **2015**, *54*, 12868-12884, doi:10.1002/anie.201501788.

27. Liu, Y.; Huang, X.; Yu, Z.; Yao, L.; Guo, S.; Zhao, W. Environmentally Friendly Non-Metal Solar Photocatalyst C3N4 for Efficient Nitrogen Fixation as Foliar Fertilizer. *ChemistrySelect* **2020**, *5*, 7720-7727, doi:10.1002/slct.202001971.
28. Dandia, A.; Gupta, S.L.; Saini, P.; Sharma, R.; Meena, S.; Parewa, V. Structure couture and appraisal of catalytic activity of carbon nitride (g-C3N4) based materials towards sustainability. *Current Research in Green and Sustainable Chemistry* **2020**, *3*, 100039-100039, doi:https://doi.org/10.1016/j.crgsc.2020.100039.
29. Xiang, Q.; Yu, J.; Jaroniec, M. Preparation and Enhanced Visible-Light Photocatalytic H2-Production Activity of Graphene/C3N4 Composites. *The Journal of Physical Chemistry C* **2011**, *115*, 7355-7363, doi:10.1021/jp200953k.
30. Hou, Y.; Laursen, A.B.; Zhang, J.; Zhang, G.; Zhu, Y.; Wang, X.; Dahl, S.; Chorkendorff, I. Layered Nanojunctions for Hydrogen-Evolution Catalysis. *Angewandte Chemie International Edition* **2013**, *52*, 3621-3625, doi:https://doi.org/10.1002/anie.201210294.
31. Yan, H.; Yang, H. TiO2–g-C3N4 composite materials for photocatalytic H2 evolution under visible light irradiation. *Journal of Alloys and Compounds* **2011**, *509*, L26-L29, doi:https://doi.org/10.1016/j.jallcom.2010.09.201.
32. Sun, J.-X.; Yuan, Y.-P.; Qiu, L.-G.; Jiang, X.; Xie, A.-J.; Shen, Y.-H.; Zhu, J.-F. Fabrication of composite photocatalyst g-C3N4–ZnO and enhancement of photocatalytic activity under visible light. *Dalton Transactions* **2012**, *41*, 6756-6763, doi:10.1039/C2DT12474B.
33. Fu, J.; Chang, B.; Tian, Y.; Xi, F.; Dong, X. Novel C3N4–CdS composite photocatalysts with organic–inorganic heterojunctions: in situ synthesis, exceptional activity, high stability and photocatalytic mechanism. *Journal of Materials Chemistry A* **2013**, *1*, 3083-3090, doi:10.1039/C2TA00672C.
34. Kowalkińska, M.; Fiszka Borzyszkowska, A.; Grzegórska, A.; Karczewski, J.; Głuchowski, P.; Łapiński, M.; Sawczak, M.; Zielińska-Jurek, A. Pilot-Scale Studies of WO3/S-Doped g-C3N4 Heterojunction toward Photocatalytic NOx Removal. *Materials* **2022**, *15*, doi:10.3390/ma15020633.
35. Liu, C.; Dong, X.; Hao, Y.; Wang, X.; Ma, H.; Zhang, X. A novel supramolecular preorganization route for improving g-C3N4/g-C3N4 metal-free homojunction photocatalysis. *New Journal of Chemistry* **2017**, *41*, 11872-11880, doi:10.1039/C7NJ02639K.
36. Dong, F.; Zhao, Z.; Xiong, T.; Ni, Z.; Zhang, W.; Sun, Y.; Ho, W.-K. In Situ Construction of g-C3N4/g-C3N4 Metal-Free Heterojunction for Enhanced Visible-Light Photocatalysis. *ACS Applied Materials & Interfaces* **2013**, *5*, 11392-11401, doi:10.1021/am403653a.
37. Schwinghammer, K.; Tuffy, B.; Mesch, M.B.; Wirnhier, E.; Martineau, C.; Taulelle, F.; Schnick, W.; Senker, J.; Lotsch, B.V. Triazine-based Carbon Nitrides for Visible-Light-Driven Hydrogen Evolution. *Angewandte Chemie International Edition* **2013**, *52*, 2435-2439, doi:https://doi.org/10.1002/anie.201206817.
38. Zhang, M.; Jiang, W.; Liu, D.; Wang, J.; Liu, Y.; Zhu, Y.; Zhu, Y. Photodegradation of phenol via C3N4-agar hybrid hydrogel 3D photocatalysts with free separation. *Applied Catalysis B: Environmental* **2016**, *183*, 263-268, doi:https://doi.org/10.1016/j.apcatb.2015.10.049.
39. Wang, Y.; Li, H.; Yao, J.; Wang, X.; Antonietti, M. Synthesis of boron doped polymeric carbon nitride solids and their use as metal-free catalysts for aliphatic C–H bond oxidation. *Chemical Science* **2011**, *2*, 446-450, doi:10.1039/C0SC00475H.
40. Shiraishi, Y.; Kanazawa, S.; Sugano, Y.; Tsukamoto, D.; Sakamoto, H.; Ichikawa, S.; Hirai, T. Highly Selective Production of Hydrogen Peroxide on Graphitic Carbon Nitride (g-C3N4) Photocatalyst Activated by Visible Light. *ACS Catalysis* **2014**, *4*, 774-780, doi:10.1021/cs401208c.
41. Zhu, J.; Wei, Y.; Chen, W.; Zhao, Z.; Thomas, A. Graphitic carbon nitride as a metal-free catalyst for NO decomposition. *Chemical Communications* **2010**, *46*, 6965-6967, doi:10.1039/C0CC01432J.

42. Liu, J.; Wang, H.; Chen, Z.P.; Moehwald, H.; Fiechter, S.; van de Krol, R.; Wen, L.; Jiang, L.; Antonietti, M. Microcontact-Printing-Assisted Access of Graphitic Carbon Nitride Films with Favorable Textures toward Photoelectrochemical Application. *Advanced Materials* **2015**, *27*, 712-718, doi:https://doi.org/10.1002/adma.201404543.
43. Dong, G.; Ho, W.; Li, Y.; Zhang, L. Facile synthesis of porous graphene-like carbon nitride (C6N9H3) with excellent photocatalytic activity for NO removal. *Applied Catalysis B: Environmental* **2015**, *174-175*, 477-485, doi:https://doi.org/10.1016/j.apcatb.2015.03.035.
44. Liang, Q.; Huang, Z.-H.; Kang, F.; Yang, Q.-H. Facile Synthesis of Crystalline Polymeric Carbon Nitrides with an Enhanced Photocatalytic Performance under Visible Light. *ChemCatChem* **2015**, *7*, 2897-2902, doi:https://doi.org/10.1002/cctc.201500076.
45. Li, G.; Lian, Z.; Wang, W.; Zhang, D.; Li, H. Nanotube-confinement induced size-controllable g-C3N4 quantum dots modified single-crystalline TiO2 nanotube arrays for stable synergetic photoelectrocatalysis. *Nano Energy* **2016**, *19*, 446-454, doi:https://doi.org/10.1016/j.nanoen.2015.10.011.
46. Bian, J.; Li, Q.; Huang, C.; Li, J.; Guo, Y.; Zaw, M.; Zhang, R.-Q. Thermal vapor condensation of uniform graphitic carbon nitride films with remarkable photocurrent density for photoelectrochemical applications. *Nano Energy* **2015**, *15*, 353-361, doi:https://doi.org/10.1016/j.nanoen.2015.04.012.
47. Liu, J.; Li, W.; Duan, L.; Li, X.; Ji, L.; Geng, Z.; Huang, K.; Lu, L.; Zhou, L.; Liu, Z.; et al. A Graphene-like Oxygenated Carbon Nitride Material for Improved Cycle-Life Lithium/Sulfur Batteries. *Nano Letters* **2015**, *15*, 5137-5142, doi:10.1021/acs.nanolett.5b01919.
48. Song, X.; Hu, Y.; Zheng, M.; Wei, C. Solvent-free in situ synthesis of g-C3N4/{001}TiO2 composite with enhanced UV- and visible-light photocatalytic activity for NO oxidation. *Applied Catalysis B: Environmental* **2016**, *182*, 587-597, doi:https://doi.org/10.1016/j.apcatb.2015.10.007.
49. Antonetti, E.; Iaquaniello, G.; Salladini, A.; Spadaccini, L.; Perathoner, S.; Centi, G. Waste-to-Chemicals for a Circular Economy: The Case of Urea Production (Waste-to-Urea). *ChemSusChem* **2017**, *10*, 912-920, doi:10.1002/cssc.201601555.
50. Xiao, J.; Xie, Y.; Nawaz, F.; Wang, Y.; Du, P.; Cao, H. Dramatic coupling of visible light with ozone on honeycomb-like porous g-C3N4 towards superior oxidation of water pollutants. *Applied Catalysis B: Environmental* **2016**, *183*, 417-425, doi:https://doi.org/10.1016/j.apcatb.2015.11.010.
51. Yu, J.; Wang, K.; Xiao, W.; Cheng, B. Photocatalytic reduction of CO2 into hydrocarbon solar fuels over g-C3N4–Pt nanocomposite photocatalysts. *Physical Chemistry Chemical Physics* **2014**, *16*, 11492-11501, doi:10.1039/C4CP00133H.
52. Zhang, G.; Zhang, J.; Zhang, M.; Wang, X. Polycondensation of thiourea into carbon nitride semiconductors as visible light photocatalysts. *Journal of Materials Chemistry* **2012**, *22*, 8083-8091, doi:10.1039/C2JM00097K.
53. Wang, K.; Li, Q.; Liu, B.; Cheng, B.; Ho, W.; Yu, J. Sulfur-doped g-C3N4 with enhanced photocatalytic CO2-reduction performance. *Applied Catalysis B: Environmental* **2015**, *176-177*, 44-52, doi:https://doi.org/10.1016/j.apcatb.2015.03.045.
54. Cui, Y.; Zhang, G.; Lin, Z.; Wang, X. Condensed and low-defected graphitic carbon nitride with enhanced photocatalytic hydrogen evolution under visible light irradiation. *Applied Catalysis B: Environmental* **2016**, *181*, 413-419, doi:https://doi.org/10.1016/j.apcatb.2015.08.018.
55. Niu, Y.; Hu, F.; Xu, H.; Zhang, S.; Song, B.; Wang, H.; Li, M.; Shao, G.; Wang, H.; Lu, H. Exploration for high performance g-C3N4 photocatalyst from different precursors. *Materials Today Communications* **2023**, *34*, 105040, doi:https://doi.org/10.1016/j.mtcomm.2022.105040.
56. Zhu, B.; Cheng, B.; Fan, J.; Ho, W.; Yu, J. g-C3N4-Based 2D/2D Composite Heterojunction Photocatalyst. *Small Structures* **2021**, *2*, 2100086, doi:https://doi.org/10.1002/sstr.202100086.

57. Tan, S.; Xing, Z.; Zhang, J.; Li, Z.; Wu, X.; Cui, J.; Kuang, J.; Yin, J.; Zhou, W. Meso-g-C3N4/g-C3N4 nanosheets laminated homojunctions as efficient visible-light-driven photocatalysts. *International Journal of Hydrogen Energy* **2017**, *42*, 25969-25979, doi:https://doi.org/10.1016/j.ijhydene.2017.08.202.
58. Dong, F.; Ni, Z.; Li, P.; Wu, Z. A general method for type I and type II g-C3N4/g-C3N4 metal-free isotype heterostructures with enhanced visible light photocatalysis. *New Journal of Chemistry* **2015**, *39*, 4737-4744, doi:10.1039/C5NJ00351B.
59. Fan, X.; Xing, Z.; Shu, Z.; Zhang, L.; Wang, L.; Shi, J. Improved photocatalytic activity of g-C3N4 derived from cyanamide–urea solution. *RSC Advances* **2015**, *5*, 8323-8328, doi:10.1039/C4RA16362A.
60. Oladoye, P.O.; Ajiboye, T.O.; Omotola, E.O.; Oyewola, O.J. Methylene blue dye: Toxicity and potential elimination technology from wastewater. *Results in Engineering* **2022**, *16*, 100678, doi:https://doi.org/10.1016/j.rineng.2022.100678.
61. Fang, H.-B.; Luo, Y.; Zheng, Y.-Z.; Ma, W.; Tao, X. Facile Large-Scale Synthesis of Urea-Derived Porous Graphitic Carbon Nitride with Extraordinary Visible-Light Spectrum Photodegradation. *Industrial & Engineering Chemistry Research* **2016**, *55*, 4506-4514, doi:10.1021/acs.iecr.6b00041.
62. Liao, G.; Yao, W. Facile synthesis of porous isotype heterojunction g-C3N4 for enhanced photocatalytic degradation of RhB under visible light. *Diamond and Related Materials* **2022**, *128*, 109227, doi:https://doi.org/10.1016/j.diamond.2022.109227.
63. Yu, X.; Fan, T.; Chen, W.; Chen, Z.; Dong, Y.; Fan, H.; Fang, W.; Yi, X. Self-hybridized coralloid graphitic carbon nitride deriving from deep eutectic solvent as effective visible light photocatalysts. *Carbon* **2019**, *144*, 649-658, doi:https://doi.org/10.1016/j.carbon.2018.12.104.
64. Fina, F.; Callear, S.K.; Carins, G.M.; Irvine, J.T.S. Structural investigation of graphitic carbon nitride via XRD and neutron diffraction. *Chemistry of Materials* **2015**, *27*, 2612-2618, doi:10.1021/acs.chemmater.5b00411.
65. Li, X.; Zhang, J.; Shen, L.; Ma, Y.; Lei, W.; Cui, Q.; Zou, G. Preparation and characterization of graphitic carbon nitride through pyrolysis of melamine. *Applied Physics A: Materials Science and Processing* **2009**, *94*, 387-392, doi:10.1007/s00339-008-4816-4.
66. Yuan, Y.; Zhang, L.; Xing, J.; Utama, M.I.B.; Lu, X.; Du, K.; Li, Y.; Hu, X.; Wang, S.; Genç, A.; et al. High-yield synthesis and optical properties of g-C3N4. *Nanoscale* **2015**, *7*, 12343-12350, doi:10.1039/c5nr02905h.
67. Cao, Y.; Wu, W.; Wang, S.; Peng, H.; Hu, X.; Yu, Y. Monolayer g-C3N4 Fluorescent Sensor for Sensitive and Selective Colorimetric Detection of Silver ion from Aqueous Samples. *Journal of Fluorescence* **2016**, *26*, 739-744, doi:10.1007/s10895-016-1764-9.
68. Liu, J.; Zhang, T.; Wang, Z.; Dawson, G.; Chen, W. Simple pyrolysis of urea into graphitic carbon nitride with recyclable adsorption and photocatalytic activity. *Journal of Materials Chemistry* **2011**, *21*, 14398-14401, doi:10.1039/C1JM12620B.
69. Ma, Y.; Liu, E.; Hu, X.; Tang, C.; Wan, J.; Li, J.; Fan, J. A simple process to prepare few-layer g-C 3 N 4 nanosheets with enhanced photocatalytic activities. *Applied Surface Science* **2015**, *358*, 246-251, doi:10.1016/j.apsusc.2015.08.174.
70. Guinier, A. *X-ray diffraction in crystals, imperfect crystals, and amorphous bodies*; W.H. Freeman: San Francisco, 1963.
71. Alizadeh, T.; Nayeri, S.; Hamidi, N. Graphitic carbon nitride (g-C3N4)/graphite nanocomposite as an extraordinarily sensitive sensor for sub-micromolar detection of oxalic acid in biological samples. *RSC Advances* **2019**, *9*, 13096-13103, doi:10.1039/C9RA00982E.
72. Galimberti, M.; Kumar, V.; Coombs, M.; Cipolletti, V.; Agnelli, S.; Pandini, S.; Conzatti, L. Filler networking of a nanographite with a high shape anisotropy and synergism with carbon black in poly(1,4-cis-isoprene) based nanocomposites. *Rubber Chemistry and Technology* **2014**, *87*, 197-218, doi:10.5254/rct.13.87903.

73. Ihlefeld, J.F.; Ginn, J.C.; Shelton, D.J.; Matias, V.; Rodriguez, M.A.; Kotula, P.G.; Carroll, J.F., III; Boreman, G.D.; Clem, P.G.; Sinclair, M.B. Crystal coherence length effects on the infrared optical response of MgO thin films. *Applied Physics Letters* **2010**, *97*, 191913, doi:10.1063/1.3515901.
74. Sing, K.S.W. Reporting physisorption data for gas/solid systems with special reference to the determination of surface area and porosity (Recommendations 1984). **1985**, *57*, 603-619, doi:doi:10.1351/pac198557040603.
75. Zinin, P.V.; Ming, L.-C.; Sharma, S.K.; Khabashesku, V.N.; Liu, X.; Hong, S.; Endo, S.; Acosta, T. Ultraviolet and near-infrared Raman spectroscopy of graphitic C3N4 phase. *Chemical Physics Letters* **2009**, *472*, 69-73, doi:https://doi.org/10.1016/j.cplett.2009.02.068.
76. Papailias, I.; Giannakopoulou, T.; Todorova, N.; Demotikali, D.; Vaimakis, T.; Trapalis, C. Effect of processing temperature on structure and photocatalytic properties of g-C3N4. *Applied Surface Science* **2015**, *358*, 278-286, doi:https://doi.org/10.1016/j.apsusc.2015.08.097.
77. Jiang, J.; Ou-yang, L.; Zhu, L.; Zheng, A.; Zou, J.; Yi, X.; Tang, H. Dependence of electronic structure of g-C3N4 on the layer number of its nanosheets: A study by Raman spectroscopy coupled with first-principles calculations. *Carbon* **2014**, *80*, 213-221, doi:https://doi.org/10.1016/j.carbon.2014.08.059.
78. Pawar, R.C.; Kang, S.; Ahn, S.H.; Lee, C.S. Gold nanoparticle modified graphitic carbon nitride/multi-walled carbon nanotube (g-C3N4/CNTs/Au) hybrid photocatalysts for effective water splitting and degradation. *RSC Advances* **2015**, *5*, 24281-24292, doi:10.1039/C4RA15560B.
79. Chaudhary, D.; Vankar, V.D.; Khare, N. Noble metal-free g-C3N4/TiO2/CNT ternary nanocomposite with enhanced photocatalytic performance under visible-light irradiation via multi-step charge transfer process. *Solar Energy* **2017**, *158*, 132-139, doi:https://doi.org/10.1016/j.solener.2017.09.012.
80. Linh, P.H.; Do Chung, P.; Van Khien, N.; Oanh, L.T.M.; Thu, V.T.; Bach, T.N.; Hang, L.T.; Hung, N.M.; Lam, V.D. A simple approach for controlling the morphology of g-C3N4 nanosheets with enhanced photocatalytic properties. *Diamond and Related Materials* **2021**, *111*, 108214, doi:https://doi.org/10.1016/j.diamond.2020.108214.
81. Groppo, E.; Bonino, F.; Cesano, F.; Damin, A.; Manzoli, M. CHAPTER 4: Raman, IR and INS Characterization of Functionalized Carbon Materials. In *RSC Catalysis Series*; 2018; Volume 2018-January, pp. 105-137.
82. Erba, A.; Desmarais, J.K.; Casassa, S.; Civalleri, B.; Donà, L.; Bush, I.J.; Searle, B.; Maschio, L.; Edith-Daga, L.; Cossard, A.; et al. CRYSTAL23: A Program for Computational Solid State Physics and Chemistry. *Journal of Chemical Theory and Computation* **2023**, *19*, 6891-6932, doi:10.1021/acs.jctc.2c00958.
83. Inoki, H.; Seo, G.; Kanai, K. Synthesis of graphitic carbon nitride under low ammonia partial pressure. *Applied Surface Science* **2020**, *534*, 147569-147569, doi:10.1016/j.apsusc.2020.147569.
84. Liu, X.; Xu, X.; Gan, H.; Yu, M.; Huang, Y. The Effect of Different g-C3N4 Precursor Nature on Its Structural Control and Photocatalytic Degradation Activity. *Catalysts* **2023**, *13*, doi:10.3390/catal13050848.
85. Liu, N.; Li, T.; Zhao, Z.; Liu, J.; Luo, X.; Yuan, X.; Luo, K.; Luo, K.; He, J.; Yu, D.; et al. From Triazine to Heptazine: Origin of Graphitic Carbon Nitride as a Photocatalyst. *ACS Omega* **2020**, *5*, 12557-12567, doi:10.1021/acsomega.0c01607.
86. Lotsch, B.V.; Döblinger, M.; Sehnert, J.; Seyfarth, L.; Senker, J.; Oeckler, O.; Schnick, W. Unmasking melon by a complementary approach employing electron diffraction, solid-state NMR spectroscopy, and theoretical calculations - Structural characterization of a carbon nitride polymer. *Chemistry - A European Journal* **2007**, *13*, 4969-4980, doi:10.1002/chem.200601759.

87. Costa, L.; Camino, G. Thermal behaviour of melamine. *Journal of thermal analysis* **1988**, *34*, 423-429, doi:10.1007/BF01913181.
88. Yan, S.C.; Li, Z.S.; Zou, Z.G. Photodegradation performance of g-C3N4 fabricated by directly heating melamine. *Langmuir* **2009**, *25*, 10397-10401, doi:10.1021/la900923z.
89. Wei, W.; Jacob, T. Strong excitonic effects in the optical properties of graphitic carbon nitride g-C3N4 from first principles. *Physical Review B - Condensed Matter and Materials Physics* **2013**, *87*, 1-7, doi:10.1103/PhysRevB.87.085202.
90. Wu, P.; Wang, J.; Zhao, J.; Guo, L.; Osterloh, F.E. Structure defects in g-C3N4 limit visible light driven hydrogen evolution and photovoltage. *Journal of Materials Chemistry A* **2014**, *2*, 20338-20344, doi:10.1039/c4ta04100c.
91. Wang, S.; Li, C.; Wang, T.; Zhang, P.; Li, A.; Gong, J. Controllable synthesis of nanotube-type graphitic C3N 4 and their visible-light photocatalytic and fluorescent properties. *Journal of Materials Chemistry A* **2014**, *2*, 2885-2890, doi:10.1039/c3ta14576j.
92. Dong, G.; Zhang, Y.; Pan, Q.; Qiu, J. A fantastic graphitic carbon nitride (g-C3N4) material: Electronic structure, photocatalytic and photoelectronic properties. *Journal of Photochemistry and Photobiology C: Photochemistry Reviews* **2014**, *20*, 33-50, doi:10.1016/j.jphotochemrev.2014.04.002.
93. Wang, J.; Hao, D.; Ye, J.; Umezawa, N. Determination of Crystal Structure of Graphitic Carbon Nitride: Ab Initio Evolutionary Search and Experimental Validation. *Chemistry of Materials* **2017**, *29*, 2694-2707, doi:10.1021/acs.chemmater.6b02969.
94. Martha, S.; Nashim, A.; Parida, K.M. Facile synthesis of highly active g-C3N4 for efficient hydrogen production under visible light. *Journal of Materials Chemistry A* **2013**, *1*, 7816-7824, doi:10.1039/c3ta10851a.
95. Chubenko, E.B.; Baglov, A.V.; Leonenya, M.S.; Yablonskii, G.P.; Borisenko, V.E. Structure of Photoluminescence Spectra of Oxygen-Doped Graphitic Carbon Nitride. *Journal of Applied Spectroscopy* **2020**, *87*, 9-14, doi:10.1007/s10812-020-00954-y.
96. Chubenko, E.B.; Kovalchuk, N.G.; Komissarov, I.V.; Borisenko, V.E. Chemical Vapor Deposition of 2D Crystallized g-C3N4 Layered Films. *The Journal of Physical Chemistry C* **2022**, *126*, 4710-4714, doi:10.1021/acs.jpcc.1c10561.
97. Zhang, Y.; Pan, Q.; Chai, G.; Liang, M.; Dong, G.; Zhang, Q.; Qiu, J. Synthesis and luminescence mechanism of multicolor-emitting g-C3N4 nanopowders by low temperature thermal condensation of melamine. *Scientific Reports* **2013**, *3*, 1943, doi:10.1038/srep01943.
98. Das, D.; Shinde, S.L.; Nanda, K.K. Temperature-Dependent Photoluminescence of g-C3N4: Implication for Temperature Sensing. *ACS Applied Materials & Interfaces* **2016**, *8*, 2181-2186, doi:10.1021/acsami.5b10770.
99. Wang, B.B.; Cheng, Q.J.; Wang, L.H.; Zheng, K.; Ostrikov, K. The effect of temperature on the mechanism of photoluminescence from plasma-nucleated, nitrogenated carbon nanotips. *Carbon* **2012**, *50*, 3561-3571, doi:https://doi.org/10.1016/j.carbon.2012.03.028.
100. Wang, K.; Zhang, Y.; Liu, L.; Lu, N.; Zhang, Z. BiOBr nanosheets-decorated TiO2 nanofibers as hierarchical p–n heterojunctions photocatalysts for pollutant degradation. *Journal of Materials Science* **2019**, *54*, 8426-8435, doi:10.1007/s10853-019-03466-z.
101. Ollis, D.F. Kinetics of Photocatalyzed Reactions: Five Lessons Learned. *Frontiers in Chemistry* **2018**, *6*, doi:10.3389/fchem.2018.00378.
102. Zhao, Z.; Sun, Y.; Luo, Q.; Dong, F.; Li, H.; Ho, W.-K. Mass-Controlled Direct Synthesis of Graphene-like Carbon Nitride Nanosheets with Exceptional High Visible Light Activity. Less is Better. *Scientific Reports* **2015**, *5*, 14643, doi:10.1038/srep14643.

Graphical abstract: